Contents lists available at ScienceDirect

Bioactive Materials

journal homepage: www.keaipublishing.com/en/journals/bioactive-materials

Harnessing the synergy of perfusable muscle flap matrix and adipose-derived stem cells for prevascularization and macrophage polarization to reconstruct volumetric muscle loss

Qixu Zhang [a,*], Yulun Chiu [b], Youbai Chen [a,c], Yewen Wu [a], Lina W. Dunne [a], Rene D. Largo [a], Edward I. Chang [a], David M. Adelman [a], Mark V. Schaverien [a], Charles E. Butler [a]

[a] Department of Plastic Surgery, The University of Texas MD Anderson Cancer Center, Houston, TX, 77030, USA
[b] Department of Melanoma Medical Oncology, The University of Texas MD Anderson Cancer Center, Houston, TX, 77030, USA
[c] Department of Plastic Surgery, Chinese PLA General Hospital, Beijing, 100853, China

ARTICLE INFO

ABSTRACT

Muscle flaps must have a strong vascular network to support a large tissue volume and ensure successful engraftment. We developed porcine stomach musculofascial flap matrix (PDSF) comprising extracellular matrix (ECM) and intact vasculature. PDSF had a dominant vascular pedicle, microcirculatory vessels, a nerve network, well-retained 3-dimensional (3D) nanofibrous ECM structures, and no allo- or xenoantigenicity. In-depth proteomic analysis demonstrated that PDSF was composed of core matrisome proteins (e.g., collagens, glycoproteins, proteoglycans, and ECM regulators) that, as shown by Gene Ontology term enrichment analysis, are functionally related to musculofascial biological processes. Moreover, PDSF−human adipose-derived stem cell (hASC) synergy not only induced monocytes towards IL-10−producing M2 macrophage polarization through the enhancement of hASCs' paracrine effect but also promoted the proliferation and interconnection of both human skeletal muscle myoblasts (HSMMs) and human umbilical vein endothelial cells (HUVECs) in static triculture conditions. Furthermore, PDSF was successfully prevascularized through a dynamic perfusion coculture of hASCs and HUVECs, which integrated with PDSF and induced the maturation of vascular networks *in vitro*. In a xenotransplantation model, PDSF demonstrated myoconductive and immunomodulatory properties associated with the predominance of M2 macrophages and regulatory T cells. In a volumetric muscle loss (VML) model, prevascularized PDSF augmented neovascularization and constructive remodeling, which was characterized by the predominant infiltration of M2 macrophages and significant musculofascial tissue formation. These results indicate that hASCs' integration with PDSF enhances the cells' dual function in immunomodulation and angiogenesis. Owing in part to this PDSF-hASC synergy, our platform shows promise for vascularized muscle flap engineering for VML reconstruction.

1. Introduction

Volumetric muscle loss (VML) resulting from traumatic injury or tumor resection often requires surgical reconstruction with autologous muscle flaps. However, this approach is often limited by a lack of high-quality autologous flaps and by donor site morbidity. One alternative strategy is to use allogenic tissue flaps, as is done in vascularized composite tissue allotransplantation [1–3]. Unfortunately, patients who undergo vascularized composite tissue allotransplantation must use immunosuppressants, many of which carry a risk for neoplasms, opportunistic infections, and/or end-organ toxicity [4]. To overcome these challenges, researchers have turned to the use of tissue-engineered skeletal muscle (TESM), in which the native structure of the muscle is reproduced *in vitro* and the engineered tissue is transplanted into the damaged area, thereby avoiding the removal of a muscle flap at a donor site [5]. Creating TESM whose thickness exceeds 1 mm requires perfusion of the construct to avoid the cell death caused by a lack of oxygen and nutrients [6]. However, one of the major shortcomings of TESM is its

---

lack of a functional vascular structure, which limits its size and thus its application in the reconstruction of VML [5–8]. Conquering this major obstacle to the successful application of TESM requires the conceptualization of vascularized composite muscle flap engineering. A vascularized composite muscle flap can be sustained by its own microcirculatory network following its microsurgical anastomosis with the host circulatory system and thus could provide a clinically viable alternative to both autologous flaps and allogenic tissue flaps.

Like whole-organ tissue engineering, which uses decellularized extracellular matrix (ECM) scaffolds derived from organs such as the heart, lung, and liver [9–11], vascularized composite tissue engineering is a recent development. In one study, researchers decellularized a segment of porcine small bowel, along with its artery and vein structure, and repopulated it with multiple types of cells *in vitro* [12]. This kind of bioartificial vascularized scaffold demonstrated functional perfusion for 1 h to 3 h in a porcine model [13] and, through the use of bypass circulation, viability for 1 week in a patient's arm [14]. Aubin et al. established a rat decellularized cardiac tissue flap that could be re-endothelialized *in vitro* [15].

Skin tissue flaps are the workhorses of routine reconstructive microsurgery. Studies have shown that acellular skin flap matrix from small animal sources retains its vascular structure [16,17]. Our own group demonstrated that a recellularized acellular skin/adipose flap resulted in significant soft tissue regeneration that was aided by vascularized transplantation via microsurgical anastomosis [18]. Researchers have also developed large-scale skin flap matrices from porcine and human cadaver sources. Those flaps had preserved structural components and vascular networks for re-endothelialization [19,20]. Jank et al. created a rat decellularized limb composite tissue matrix. The tissue matrix, recellularized with multiple cell types, showed perfusion following a short-term, non-survival procedure in a rodent model [21]. More recently, human and porcine decellularized face and ear units have been reported. All flap matrices had a 3-dimensional (3D) ECM framework and vascular tree that facilitated cells' engraftment and viability [22–24]. Overall, the use of decellularized composite tissue matrix for vascularized composite tissue engineering has progressed much in recent years. However, in-depth proteomic characterizations of acellular flap matrices are lacking, and interactions between the cells and scaffolds have not been thoroughly investigated *in vitro*. In addition, most models' remodeling processes are still in need of long-term observation *in vivo*.

Muscle ECM−based scaffolds are widely used in muscle engineering because they provide a bio-inductive platform that improves healing, as seen in an array of different VML models [25–29]. However, achieving large-scale muscle regeneration with ECM-based scaffolds alone remains a challenge. Therefore, researchers must develop new approaches that combine myogenic cells, myoconductive scaffolds, and vasculogenic activators [30]. Although vascularized composite muscle flap engineering could meet this requirement, detailed studies of muscle ECM−based flap matrices are lacking. Thus, the purpose of the present study was to establish a platform for using a perfusion-decellularization protocol to process a porcine stomach muscle flap to engineer vascularized muscle tissue that has more flexible clinical applicability. Porcine stomach muscle was selected because it is sufficiently large to provide adequate muscle tissue ECM, has a rich vascular network, has strong mechanical properties [31], and is easy to process. The porcine stomach musculofascial flap matrix (PDSF) was comprehensively characterized with respect to its 3D architecture, biomolecular patterning, proteomic profiling, and bioactivity. The biocompatibility of the PDSF was tested by integrating it with human adipose-derived stem cells (hASCs), human umbilical vein endothelial cells (HUVECs), and human skeletal muscle myoblasts (HSMMs). The immunomodulatory properties of the PDSF, either alone or seeded with hASCs, were assessed *in vitro* and *in vivo*. Prevascularized and recellularized PDSF with a dominant vascular pedicle and integrating multiple cell types was then implanted to repair VML in a full-thickness abdominal wall defect model, and the *in*

vivo response, biocompatibility, and remodeling properties of PDSF were evaluated (Scheme 1). The findings of the present study should inform the development of a platform for designing and fabricating 3D vascularized muscle tissue constructs that can be used to repair extensive musculofascial tissue defects.

2. Materials and methods

2.1. Creation of the PDSF, porcine decellularized muscle matrix, porcine decellularized fascia matrix, and human decellularized dermal matrix

All animal handling and experimental procedures strictly followed a research protocol that was approved by MD Anderson's Institutional Animal Care and Use Committee and followed National Institutes of Health (NIH) guidelines for animal welfare. Stomachs and their blood vessels were harvested from 6 euthanized 100-kg domestic female pigs. Immediately after harvest, smooth muscle flaps were raised (Fig. S1). Briefly, a parallel incision was made 5 cm from the artery pedicle, and dissection continued between the muscle and submucosa layers until the desired flap size (about $10 \times 15 \times 0.5$ cm) was achieved. Whole layers of muscle were included in the flap. The vascular pedicle included the gastroepiploic artery and accompanying vein on the greater curvature side of the stomach. The artery was catheterized with a 20G catheter (BD Biosciences, San Jose, CA), and the flap was irrigated with normal saline until clear saline flowed from the vein. The flaps were frozen at −80 °C and thawed at room temperature for 3 cycles and then processed with chemical detergents as described previously with modification [18,32]. The artery of each flap was catheterized, and the flaps were connected via the catheter to a Masterflex pump perfusion system (Cole-Parmer, Vernon Hills, IL) and perfused with ultrapure water (5–10 ml/min) for 1 day at room temperature. The flaps were then treated with 0.5 M NaCl for 4 h, 1 M NaCl for 4 h, and ultrapure water overnight; this saltwater perfusion procedure was repeated once. After they were treated with 0.25% trypsin/ethylenediaminetetraacetic acid (EDTA) for 2 h at 37 °C and washed with deionized water for 1 h, the flaps were processed with isopropanol overnight with agitation. The flaps were then treated with 1% Triton X-100 for 2 days (1 change daily), washed in ultrapure water for 2 days (3 changes daily), and rinsed in phosphate-buffered saline (PBS) for 1 day within the perfusion system. The decellularization cycle was repeated 2 times. Any vessel branches with open ends were clamped to prevent leaking. PDSF was then sterilized with 70% ethanol, rinsed in PBS, and stored in PBS at 4 °C until use. Rat decellularized abdominal wall muscle flap matrix (RDMF) was used as a positive control *in vivo*. Rat native skeletal muscle (RNM) based on the deep inferior epigastric artery and vein was harvested from 8-week-old male Fischer 344 rats (Harlan Laboratories, Indianapolis, IN) and then decellularized using same perfusion protocol used for PDSF.

To better characterize PDSF, we compared it with porcine decellularized muscle matrix (PDMM), porcine decellularized fascia matrix (PDFM), and human decellularized dermal matrix (HDDM). Porcine anterior rectus musculofascial tissue was harvested from donor pigs. Samples of skin tissues resected from the abdominal wall of a patient undergoing reconstructive surgery were collected. All procedures involving human tissue samples were approved by MD Anderson's Institutional Review Board and conducted in accordance with MD Anderson's research guidelines. PDMM, PDFM, and HDDM were prepared as described previously [32]. All decellularization steps were carried out at room temperature (except as indicated) with agitation (120 rpm). First, the samples were frozen at −80 °C, then thawed at room temperature for 3 cycles, and then washed in ultrapure water for 2 days. The washed samples were treated with 0.5 M NaCl for 4 h, treated with 1 M NaCl for 4 h, and then washed in ultrapure water overnight; this procedure was repeated once. After being treated with 0.25% trypsin/EDTA at 37 °C for 2 h, the samples were washed in deionized water for 1 h. The samples were treated with 1% Triton X-100 for 5 days (1 change daily), processed with DNAase at 37 °C for 3 h, washed in
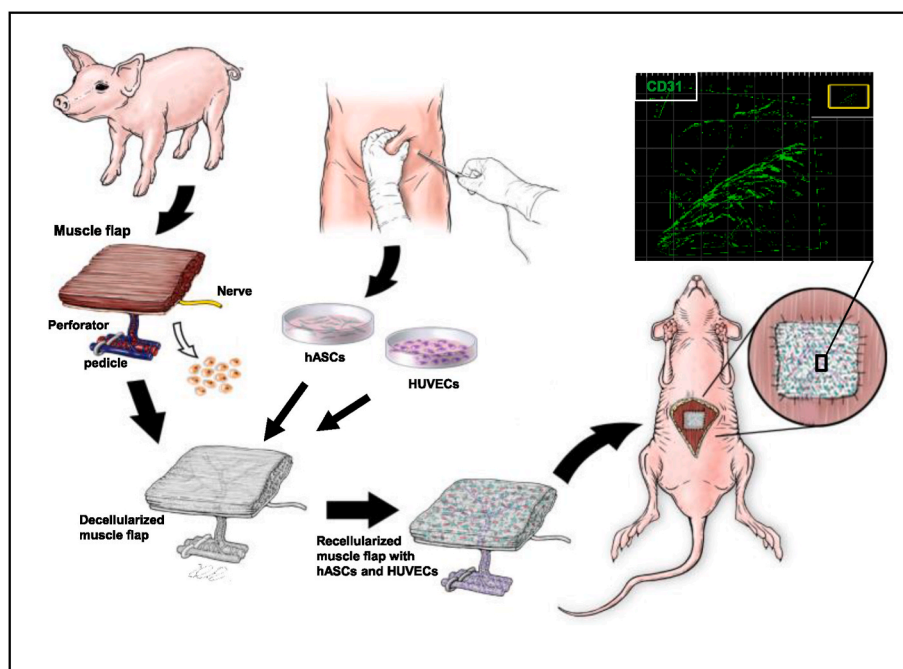
Scheme 1. Prevascularized PDSF (engineered muscle flap) with a co-culture of human adipose-derived stem cells (hASCs) and human umbilical vein endothelial cells (HUVECs) was transplanted into a recipient nude rat for VML reconstruction. The inset image indicates the prevascularized area shown in the magnified view.

ultrapure water for 2 days, and rinsed in PBS for 1 day. This decellularization process was repeated 3 times. PDMM, PDFM, and HDDM were then sterilized using 70% ethanol, rinsed in PBS, and stored in PBS at 4 °C until use.

2.2. Characterization of PDSF

2.2.1. DNA assessment and quantification

Cell removal was quantified by measuring the nucleic acid concentration with the Quant-iT PicoGreen dsDNA assay kit (Molecular Probes, Eugene, OR) as described previously [32]. Briefly, native tissues and decellularized samples (n = 6 each) were lyophilized and digested in 1 mg/ml papain (Sigma, St. Louis, MO) at 60 °C for 48 h. The samples were then centrifuged at 12,000 rpm at 4 °C for 10–15 min. Fluorescence intensity in the supernatants was measured using a VersaFluor spectrofluorometer (BioRad Laboratories, Hercules, CA), and the measured DNA quantity was normalized to the initial dry weight of the tissue.

2.2.2. Sulfated glycosaminoglycan content

The sulfated glycosaminoglycan (GAG) content of the native tissues and decellularized samples was quantified using an Alcian blue colorimetric assay kit (sGAG Dye Binding Assay, ALPCO, Salem, NH) [32]. Samples were lyophilized, digested with papain, and then incubated with Alcian blue dye. Absorbance of the samples at 600–620 nm was measured with a DU 730 UV/Vis scanning spectrophotometer (Beckman Coulter, Brea, CA) using chondroitin sulfate (Sigma) as the standard. GAG content was normalized to the initial dry weight of the samples (n = 6 each).

2.2.3. Mechanical properties assessment

The mechanical properties of the PDSF samples (average dimension, 5.11 × 2.39 × 5 mm [width × thickness × distance between clamps]; n = 6) were determined by uniaxial tensile testing using the ElectroForce 3200 system (Bose Corporation, Minnetonka, MN) at room temperature. Samples were cut into small strips and kept in PBS until testing. While moist, the samples were placed between 2 clamps. The widths and thicknesses of the samples were measured using an electronic digital caliper, and the cross-section area was calculated. Samples were tested with a 225-N load cell (Honeywell Sensotec, Columbus, OH) at a strain rate of 500 μm/s, and stress-strain curves were calculated. These curves were used to determine ultimate tensile strength (UTS), elastic modulus, and strain at failure. PDMM and PDFM samples served as controls (n = 6 each) [32].

2.2.4. Vascular structure measurement

The microcirculatory network of PDSF was demonstrated by injecting 2 ml of mixed Microfil-117 (Flow Tech, South Windsor, CT) solution into the artery pedicle at a rate of 1 ml/min. PDSF was stored at 4 °C overnight and then imaged using a Discovery V8 microscope (Zeiss, Oberkochen, Germany).

2.2.5. Scanning electron microscopy

PDSF samples (n = 3) were frozen at −80 °C and dried through lyophilization with a FreeZone Triad benchtop freeze dryer (Labconco, Kansas City, MO). Cells on the decellularized samples were fixed with 2% paraformaldehyde and 3% glutaraldehyde in PBS for 1 h and then rinsed in 0.1 M cacodylate buffer 3 times for 5 min each. This was followed by postfixing with 1% OsO4 in 0.1 M sodium cacodylate buffer for 1 h and rinsing in cacodylate buffer 3 times for 5 min each. The samples were then dehydrated in 35%, 50%, 70%, 80%, 95%, and 100% ethanol successively for 10 min each and dried in hexamethyldisilazane (Sigma). The dry samples were coated with a platinum alloy to a thickness of 25 nm under vacuum using a Balzer MED 010 evaporator (Technotrade International, Manchester, NH). Samples were examined with a JSM-5910 scanning electron microscope (SEM; JEOL, USA, Inc., Peabody, MA) at an accelerating voltage of 5 kV. Fiber size was measured using the ImageJ software program (NIH, Bethesda, MD).

2.2.6. Histological analysis

Porcine native stomach (PNS) muscle tissue and PDSF (n = 6 each) were fixed in 10% formalin, embedded in paraffin, and sliced into 5-μm sections, which were mounted on slides. The slides were stained with hematoxylin and eosin (H&E), Masson trichrome, and 4′,6-diamidino-2-phenylindole (DAPI). For immunohistochemical (IHC) staining, the slides were placed in antigen retrieval citrate buffer (Biogenex, Fremont, CA) in a steamer for 10 min at 95 °C. Endogenous peroxidases were

blocked by incubation with Peroxide Block (Innogenex, San Ramon, CA), and nonspecific binding was blocked with normal goat serum (Vector Laboratories, Burlingame, CA). Sections were incubated with primary antibodies against collagen I, laminin, MHC-I, MHC-II, and galactose-α-1,3-galactose (α-gal; all from Abcam, Cambridge, MA) overnight at 4 °C. The sections were washed, received an application of a biotinylated secondary antibody for 30 min, and were treated with streptavidin-horseradish peroxidase complex (using the Vectastain ABC Kit) and diaminobenzidine solution (both from Vector Laboratories) and counterstained with hematoxylin. The sample sections were dehydrated, mounted, and imaged using the Vectra multispectral slide analysis system (PerkinElmer, Waltham, MA).

2.2.7. Proteomics profiling

2.2.7.1. Protein extraction and digestion.
Fifteen-microgram samples of PNS, PDSF, PDMM, and HDDM were washed with ice-cold PBS and then pulverized, and their proteins were precipitated with acetone (acetone/sample ratio, 5:1) and stored overnight at -20 °C. The precipitated proteins were resuspended in 10 µl of RapiGest (2 mg/ml in 100 mM ammonium bicarbonate; Waters, Milford, MA) plus 30 µl of 50 mM ammonium bicarbonate and heated to 100 °C for 10 min. The samples were cooled to room temperature and digested with 200–400 ng of sequencing-grade trypsin (20 ng/µl in 0.02% formic acid; Promega, Madison, WI) at 37 °C overnight. The digested samples were dried using a SpeedVac vacuum concentrator (Thermo Fisher Scientific, Waltham, MA) and reconstituted in 1% formic acid.

2.2.7.2. Liquid chromatography–tandem mass spectrometry.
The resulting peptides were analyzed by liquid chromatography–tandem mass spectrometry (LC–MS/MS) on an Orbitrap Fusion mass spectrometer (Thermo Fisher Scientific). High-performance liquid chromatography analyses were performed with the UltimMate 3000 RSLnano system (Thermo Fisher Scientific). Samples were injected into a 150 mm × 2.7 µm core–shell C18 DB column (Phenomenex, Torrance, CA) with mobile phase compositions of 0.1% formic acid in water (composition A) and 0.1% formic acid in acetonitrile (composition B) at a flow rate of 100 µl/min. For composition B, the gradient was held in the isocratic mode at 2% for 2 min, ramped up to 35% at 165 min, ramped up to 80% at 166 min, maintained at 80% until 176 min, ramped down to 2% at 177 min, and held at 2% until 190 min. The MS parameters and scan strategy were: mass range for MS1, 400–1300; mass resolution for MS1, 500,000; mass window for precursor ion selection, 0.5 Da; number of precursors selected for tandem MS in each scan cycle, maximum in 2 s; MS1, Orbitrap; MS2, Iontrap; charge state screening parameters, 2–4; relative collision energy, 30%; and dynamic exclusion settings, 15 s.

2.2.7.3. Computational analysis of mass spectra. Database Search.
Tandem mass spectra were analyzed using the Mascot software program (version 2.5) via Proteome Discoverer (version 1.4) to search against the UniProt Homo sapiens proteome database (version 2017_12). The database contains a total of 161,521 human protein sequences. The searches were performed with a precursor ion mass tolerance of 10 ppm, a fragment ion mass tolerance of 0.8 Da with trypsin specification, and 2 missed cleavages allowed. The variable modifications included oxidation (M), Gln → pyro-Glu (N-term Q), and trioxidation (C). The IonScore cutoff was 20, and the false discovery rate was 0.1. Prior to pathway analysis, for both the native and decellularized tissues, the MS1 peak areas were defined for quantitative analysis and calculated using the Skyline software program (version 3.7.0.10952), which extracted from the Proteome Discoverer search results (.msf files) and raw data. The total peak area for all MS1 representing the same protein group was summed to represent the quantity of the protein group. The quantification for each replicate run was normalized to the mean of the total MS1 peak area of each group.

Bioinformatic Analysis. The identified proteins were further cross-referenced to the gene sets of the Matrisome Project, which is maintained by the Broad Institute. The protein-encoding gene sets were categorized as ECM glycoproteins, collagens, proteoglycans, ECM-affiliated proteins, ECM regulators, or secreted proteins. The classification rules of the MIT Matrisome Project (http://matrisomeproject.mit.edu/) were followed.

Pathway Analysis. The retained proteins from the decellularized tissues were functionally grouped by ClueGO (version 2.3.3), a Cytoscape (version 3.5.1) plug-in that visualizes the non-redundant biological terms for large clusters of genes in a functionally grouped network. The ClueGo network is created with kappa statistics and reflects the relationship between the terms based on the similarity of their associated genes. The pathways with *P*-values of less than 0.05 were reported; clusters had to have at least 2 proteins to be included in the statistical analysis.

2.3. Evaluation of hASCs' integration with PDSF

2.3.1. Seeding hASCs on PDSF
All procedures were approved by MD Anderson's Institutional Review Board and performed in accordance with the institution's research guidelines by a single surgeon. Adipose tissue samples were harvested from 3 women undergoing reconstructive surgery after mastectomy at MD Anderson. Patients provided their written informed consent to be included in the study. (The patients were 26, 35, and 37 years old, respectively; they all presented with a complaint that required reconstructive surgery, but they were otherwise healthy, and they had not received radiotherapy.) hASCs were isolated and identified according to our established protocol [33]. hASCs were cultured in α-minimum essential medium (α-MEM; Mediatech, Manassas, VA) containing 10% fetal bovine serum, 2 mM L-glutamine, 100 µg/ml penicillin, and 100 µg/ml streptomycin. hASCs within 3 passages were harvested and used in all experiments. hASCs were plated onto PDSF scaffolds at a density of 2×10^4 cells/cm^2 and then stained with calcein AM and ethidium homodimer-1 using the LIVE/DEAD Viability/Cytotoxicity Kit (Molecular Probes) according to the manufacturer's instructions. Samples were examined with an IX81 confocal fluorescence microscope (Olympus, Center Valley, PA) 1, 3, and 7 days after cell seeding (n = 3/group). Samples were also analyzed with an SEM (n = 3/group). Cell morphologic features were measured using ImageJ software.

2.3.2. Differentiation assay
A differentiation assay was used to determine the effects of PDSF's molecular components on stem cells' differentiation capacity. PDSF samples were ground into a fine powder and then incubated with α-MEM at a concentration of 0.3 g/ml (w/v) at 37 °C for 72 h with agitation. After centrifugation, the supernatant was added to adult stem cell differentiation medium (DM) from a GIBCO stem cell differentiation kit (Life Technologies, Carlsbad, CA) at a 1:3 ratio to prepare conditioned DM (CDM). hASCs were plated in 6-well plates at a density of 1×10^4 cells/cm^2 and then cultured with α-MEM, DM, or CDM for 6–10 days. The adipogenesis of hASCs was assessed by Oil-Red-O staining. Osteogenesis was assessed by Alizarin-Red-S staining. Plates were imaged using an Olympus IX71 microscope and analyzed using ImageJ software.

2.4. Assessment of the immunomodulatory effect of PDSF-hASC synergy on macrophage polarization

Four experimental groups were designed. In group 1, CD14$^+$ M0 monocytes were cultured alone; in group 2, M0 monocytes were cocultured with the PDSF scaffold; in group 3, M0 monocytes were cocultured with hASCs; and in group 4, M0 monocytes were cocultured with hASC-loaded PDSF (n = 3 biological replicates/group). In the coculture system, M0 monocytes were seeded in the wells of 6-well tissue culture polystyrene plates, and PDSF, hASCs, and hASC-loaded

PDSF were placed in well inserts (BD Falcon, Franklin Lakes, NJ). The system was maintained in culture for 7 days, and then biological analyses were performed.

2.4.1. Cell culture

Normal human CD14^{+} M0 monocytes (PCS-800-010; ATCC, Manassas, VA) were cultured in phenol red–free RPMI-1640 supplemented with 10% fetal bovine serum, 2 mM L-glutamine, 1% sodium pyruvate, and 1% non-essential amino acids. M0 monocytes (2×10^4 cells/cm^2) within 3 passages were seeded in the wells of tissue culture polystyrene plates. hASCs (2×10^4 cells/cm^2) within 3 passages were seeded on PDSF scaffold samples (2 cm in diameter), which were placed in the inserts. The coculture system was cultured with monocyte medium in a 95% humidified 5% CO_2 atmosphere for 7 days at 37 °C.

2.4.2. Flow cytometry

After 7 days of co-culture, macrophages were harvested and subjected to flow cytometry with an LSR II flow cytometer (BD Biosciences). Briefly, the resulting cell suspensions (1×10^5 cells/100 μl) were stained using antibodies against CD14 fluorescein isothiocyanate, CD16 phycoerythrin (a human M1 macrophage profile marker), CD206 allophycocyanin (a human M2 macrophage profile marker), and human leukocyte antigen–DR peridinin chlorophyll protein–Cy5.5 (BD Pharmingen, San Diego, CA). Data were analyzed using the FlowJo software program, version 10 (Tree Star, Inc., Ashland, OR). The percentages of cells within each gate were determined by comparing their numbers to those of isotype-matched controls.

2.4.3. Cytokine secretion assay

The expression levels of cytokines (interleukin [IL]-2, IL-4, IL-6, IL-8, IL-10, interferon γ [IFN-γ], tumor necrosis factor α [TNF-α], and vascular endothelial growth factor [VEGF]) in fresh medium were analyzed simultaneously using the Bio-Plex Multiplex Immunoassay System (Bio-Rad Laboratories, Hercules, CA), which is based on xMAP technology (Luminex Corporation, Austin, TX). The manufacturer's instructions were followed. xMAP follows the principles of a sandwich ELISA. In short, 50 μl of the cell-free culture supernatants of each group from days 3, 5, and 7 were incubated with 50 μl of different types of magnetic, fluorescently dyed microspheres (beads) in a 96-well microtiter plate, and each bead type was coupled to antibodies specific to the antigens of interest. A magnetic plate washer was used to repeatedly wash the samples to remove unbound proteins, and the samples were then incubated with a mix of biotinylated detection antibodies to create a bead antibody-sample antibody complex. The samples were washed again and subsequently coupled with a streptavidin-phycoerythrin conjugate, which served as the reporter to measure the quantities of the analytes of interest. The samples were then analyzed using a Bio-Plex 200 reader, which recognized each bead at 635 nm to provide bead classification and recognized phycoerythrin at 532 nm to provide quantitation for each analyte of interest. Data were analyzed with Bio-Plex Manager software (version 5.0).

2.4.4. Human growth factor array

The expression levels of growth factors (41 human proteins) in fresh medium were analyzed using a RayBio C-Series Human Growth Factor Antibody Array C1 (RayBiotech, Norcross, GA) according to the manufacturer's instructions. Briefly, 1 ml of the cell-free culture supernatant of each group from day 7 was incubated with the membrane in the well of the incubation tray at 4 °C overnight. Following repeated washing, the membrane was incubated with a biotinylated antibody cocktail for 2 h at room temperature and then with horseradish peroxidase–conjugated streptavidin for 2 h at room temperature. Then the membrane was visualized with enhanced chemiluminescence (Amersham, Arlington Heights, IL). Relative protein levels were determined by densitometry and normalized to positive controls using ImageJ software.

2.4.5. Aortic ring assay

An aortic ring assay was used to determine the effects of PDSF-hASC synergy on angiogenesis *in vitro*. Rat thoracic aortas were obtained from three 8-week-old female nude rats (NIH). The aortas were sectioned into 1-mm-thick rings, which were then immersed in 25 μl of rat-tail collagen type I (BD Biosciences) and incubated at 37 °C for 30 min to allow the collagen solution to transform into a gel. Aortic rings embedded in the collagen gels were treated with regular endothelial growth medium (EGM; Lonza, Walkersville, MD) mixed with the same volume of fresh medium collected from groups 1–4 on day 7. Phase-contrast images of these rings were taken on day 7 using an Olympus IX70 microscope. Aortic rings with cell and microvessel outgrowth were stained with a mouse monoclonal primary antibody against CD31 (1:200; AbD Sero-Tec, Raleigh, NC) and a rabbit monoclonal primary antibody against α-smooth muscle actin (1:200; Abcam) and then stained with goat anti-mouse DyLight 488 and goat anti-rabbit Dylight 594 (each 1:500; both from Jackson ImmunoResearch Laboratories, West Grove, PA). Cell nuclei were stained with DAPI (1:5000; Molecular Probes). The stained rings were viewed with an LSM 7 MP multiphoton microscope (Zeiss). Images of the rings were analyzed using Imaris 8.0 (Oxford Instruments, Abingdon, Oxfordshire, England).

2.5. Evaluation of HSMMs' integration with PDSF

2.5.1. Cell culture and seeding

HSMMs were used to test if PDSF provided a 3D microenvironment sufficient for skeletal muscle cell growth. HSMMs were cultured alone, cocultured with HUVECs, or tricultured with HUVECs and hASCs on 2-dimensional (2D) glass, 3D collagen gel, or 3D PDSF in 4-chamber culture slides (0.5 × 1 cm/chamber; BD Falcon). Cells were statically cultured for 7 and 14 days and then immunostained for analysis with 2-photon excitation microscopy (n = 6/condition).

All cells were used within 3 passages. HSMMs (Lonza) were cultured in SkGM-2 skeletal muscle growth medium. HUVECs (Lonza) were cultured in EGM according to the manufacturer's instructions. Cells were co-cultured in SkGM-2 and EGM at a 1:1 ratio. Cells were loaded onto 2D glass, 3D collagen gel, and PDSF at 2×10^4 cells/cm^2. For the 3D collagen gel culture, cells were mixed with 250 μl of rat-tail collagen type I and incubated at 37 °C for 30 min to allow the collagen solution to transform into a gel. The medium was replaced every other day, and the cultures were maintained in a 95% humidified 5% CO_2 atmosphere at 37 °C.

2.5.2. Fluorescence immunostaining

On days 7 and 14, cells on 2D glass, collagen gel, and PDSF were stained with a mouse monoclonal primary antibody against CD31 (1:200; AbD SeroTec) and a rabbit monoclonal primary antibody against desmin (1:200; Abcam) and then stained with goat anti-mouse DyLight 488 and goat anti-rabbit Dylight 594 (1:500; Jackson ImmunoResearch Laboratories). Cell nuclei were stained with DAPI (1:5000). The stained samples were viewed with 2-photon excitation microscopy and analyzed using Imaris 8.0.

2.6. Prevascularization of PDSF

The prevascularization and endothelialization of the flap matrix helps transplanted engineered flap constructs establish an early blood supply and integrate with the host. HUVECs and hASCs were cultured statically (for 1 week) and dynamically (for 2 weeks) on PDSF to optimize its prevascularization.

Three PDSF samples (each 4 × 5 cm with a 4-cm vascular pedicle) were used in the experiment. Prior to seeding, hASCs were labeled with PKH26 (Sigma) according to the manufacturer's instructions. The repopulation process followed 3 steps: 1) hASC preconditioning, 2) HUVEC repopulation, and 3) bioreactor perfusion. For hASC preconditioning, hASCs were injected into the vascular network (1×10^6 in

400 μl of α-MEM for each artery and vein system) and parenchyma (1 × 10^6 in 400 μl of medium at 10 sites) of PDSF and allowed to grow statically for 3 days. For HUVEC repopulation, half of the α-MEM was replaced with EGM, and then HUVECs were injected into the vascular network (1 × 10^6 in 400 μl of medium for each artery and vein system) and parenchyma (1 × 10^6 in 400 μl of medium at 10 sites) of PDSF and allowed to grow statically for 4 days. For bioreactor perfusion, the cell-treated PDSF was connected via catheter to a Masterflex pump perfusion system (Cole-Parmer), which perfused the PDSF with EGM containing an additional suspension of hASCs and HUVECs (1 × 10^6 of each cell type) for 3 weeks (5 ml/min for the first week and 10 ml/min for the second and third weeks) in a 95% humidified 5% CO_2 atmosphere at 37 °C.

The cell-seeded PDSF was stained with a mouse monoclonal antibody against CD31 (1:200) and then with goat anti-mouse DyLight 488 (1:500). All cells were stained with DAPI. Samples were viewed with 2-photon excitation microscopy and analyzed using Imaris 8.0.

2.7. Examination of the host reaction to PDSF in vivo

All animal procedures were approved by MD Anderson's Institutional Animal Care and Use Committee and met all requirements of the U.S. Animal Welfare Act. Eight-week-old male Fischer 344 rats (Harlan Laboratories) were anesthetized; anesthesia was induced and maintained with isoflurane (0.5%–2%, 3–5 L/min) and oxygen. Animals were divided into 5 groups (n = 6/group) on the basis of their donor grafts: 1) PDSF, 2) porcine fresh skeletal muscle (PNM), 3) porcine fresh stomach smooth muscle (PNS), 4) Fischer 344 rat native skeletal muscle (RNM), and 5) native stomach smooth muscle (RNS). Two graft samples (0.5 × 1 cm each) were implanted subcutaneously on the back of each rat. The animals were monitored for clinical signs of inflammation or rejection for 2 weeks or 4 weeks and then euthanized by CO_2 asphyxiation. Specimens were cut from the centers of the explants, fixed in 10% formalin, and embedded in paraffin. Sections cut from the paraffin-embedded samples were mounted on slides and subjected to H&E staining and Masson trichrome staining as well as IHC staining with antibodies against CD3, FoxP3, CD68, MyoD1 (all 1:200; Abcam), CD80, and CD163 (both 1:200; AbD Serotec). CD68, CD80, and CD163 are macrophage markers; CD3 and FoxP3 are lymphocyte markers; and MyoD1 is a myogenic marker. The slides were scanned using the Vectra multispectral slide analysis system. The resulting multispectral images were analyzed using the InForm Tissue Finder Advanced Image Analysis software package (PerkinElmer).

2.8. VML reconstruction with prevascularized PDSF in a full-thickness abdominal wall defect model

2.8.1. VML reconstruction with prevascularized PDSF

Full-thickness anterior abdominal wall defects (each 2 × 2 cm; ~30%–40% of the anterior abdominal wall area) were created in 8-week-old male nude rats (NIH; n = 6/group). Nude rats were used to avoid the host immunorejection of human tissue−derived hASCs and HUVECs. PDSF and prevascularized PDSF (PDSF cultured with hASCs and HUVECs for 1 week) were used for VML repair. PDSF was transplanted into the defect site with the serosa side facing the peritoneum and the muscularis side facing the skin. The tissue-graft interface was sutured with 5-0 Prolene sutures (Ethicon, Somerville, NJ) in a running pattern. This repair resulted in the bridging of the elliptical muscu-lofascial defect (2 × 2 cm) by the PDSF graft, with a 0.5-cm peripheral zone of implant–musculofascial layer overlap. The skin was closed with absorbable subcutaneous 5-0 Vicryl sutures (Ethicon). Animals were monitored until they fully recovered from anesthesia. Animals were euthanized for sample explantation 1 or 3 months after surgery. RDMF was used as a positive control to repair full-thickness abdominal wall defects (0.5 × 0.5 cm) in 3 nude rats; samples were explanted 3 months after surgery.

2.8.2. Gross evaluation

Rats were euthanized with CO_2. The entire abdominal wall was circumferentially incised to widely expose the repair site for analysis without disrupting any abdominal adhesions. After the repair site was photographed, it was evaluated by 3 independent observers blinded to the rat's group. A gross evaluation of adhesion structures and adhesion grade and strength at each repair site was performed. Briefly, the adhesion structures examined included the omentum, bowel, stomach, and liver. The adhesion coverage area was quantified as a percentage of the total visible implant area that was taken up by adhesions. Adhesions were graded according to the Butler adhesion scale, a 0–3 scale with intervals of 0.5, in which 0 represents no adhesions, 1 represents adhesions easily freed with gentle force, 2 represents adhesions freed with blunt dissection, and 3 represents adhesions requiring sharp dissection to be freed from the implant site [34].

2.8.3. Mechanical test

After the entire abdominal wall was removed, it was cut into 3 strips. The center strip was used for the mechanical test, and the other 2 strips were fixed for histological analysis. For the mechanical test, the sample was covered in saline-wetted gauze and placed on ice. All sutures were removed before mechanical testing; all samples were measured within 4 h of harvesting and tested at room temperature while moist. For the assessment of the interfacial strength between the muscle and the remodeled graft, strips were cut from the middle of the graft. One clamp was placed on one end of the abdominal wall, and the other was placed on the explant graft at the other end of the abdominal wall, thereby placing the interfacial area in the center between the 2 clamps (average dimension, 4.48 × 2.11 × 5 mm [width × thickness × distance between clamps]; n = 6/group). The area where sutures were removed was considered the interface. The mechanical properties at the implant-musculofascial interface were measured as described in section 2.2.3.

2.8.4. Evaluation of blood perfusion

For the evaluation of functional neovascularization in a PDSF graft, fluorescein-labeled dextran (70,000 MW; Life Technologies, Grand Island, NY) was diluted in PBS (25 mg/ml), and 500 μl of the dextran solution was injected through the tail vein with the rat under general anesthesia. Circulating dextran in the vascular system of the explanted graft was imaged with an Olympus IX81 confocal fluorescence microscope immediately thereafter (n = 3/group).

2.8.5. Evaluation of tissue remodeling and musculofascial regeneration

The explanted grafts were fixed in 10% formalin and embedded in paraffin. Sections cut from the paraffin-embedded samples were subjected to H&E staining and Masson trichrome staining as well as IHC staining for CD31, CD68, MyoD1, and desmin (all 1:200; Abcam); CD80 and CD163 (both 1:200; AbD Serotec); and human nuclear antigen (HuNu; 1:200; Millipore, Bedford, MA). The slides were imaged and analyzed using the Vectra multispectral slide analysis system. The details of using the ABC kit for IHC staining are described in section 2.2.6.

2.9. Statistical analysis

Data were presented as means ± standard errors of the means. Data were analyzed using one-way analysis of variance and the Student t-test with the SigmaStat software program (version 3.5, SyStat). P-values of less than 0.05 were considered significant.

3. Results

3.1. PDSF provides a 3D composite musculofascial flap matrix with intact vasculature

The musculofascial layer of the stomach samples turned from peach-pink to white after decellularization (Fig. 1A–G). The mean thickness of
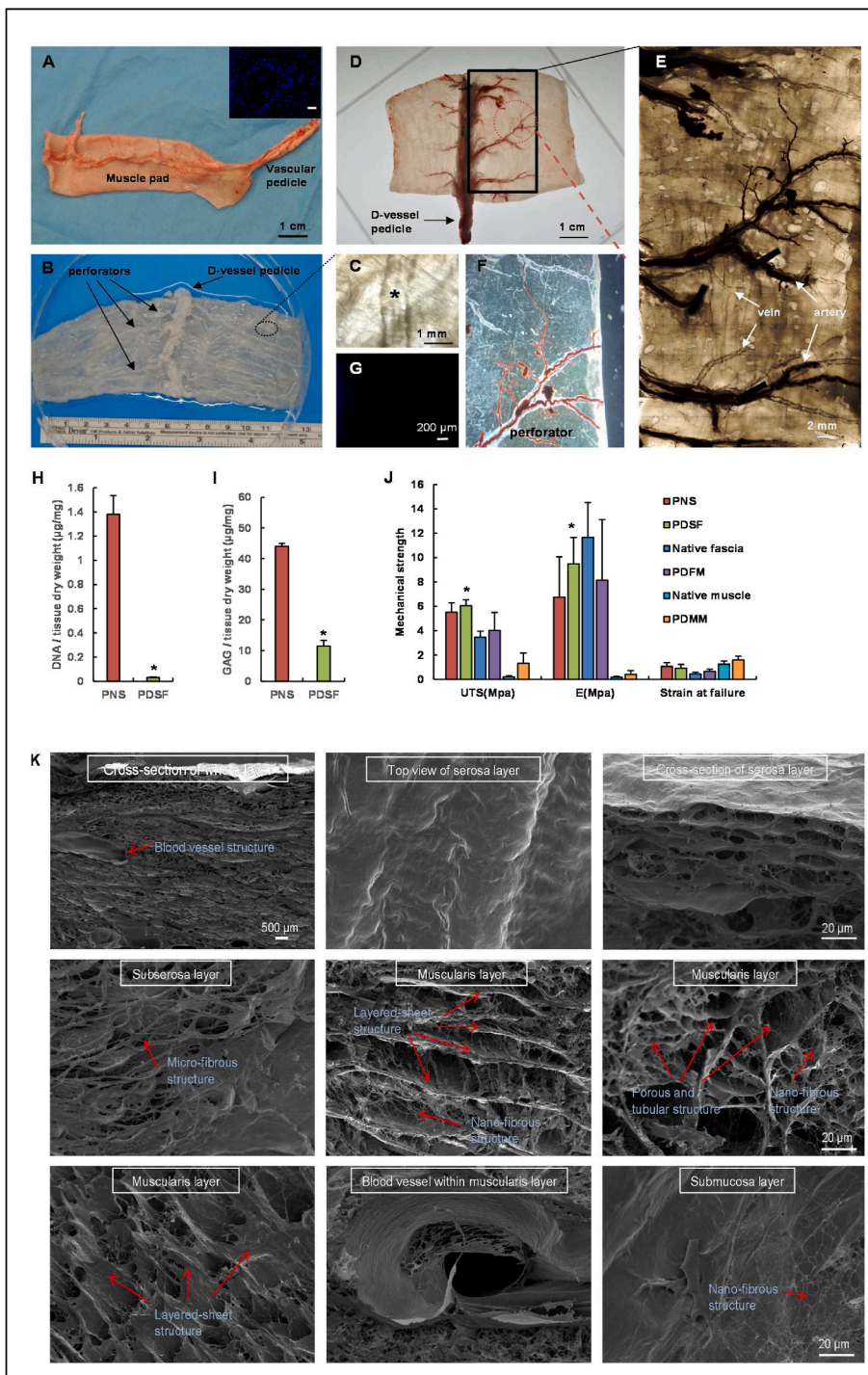
Fig. 1. Perfusion decellularization and flap matrix angiography. (A) A porcine stomach musculofascial flap with gastric blood vessels. The inset image shows nuclear DNA stained by DAPI (scale bar = 200 μm). (B) A transparent PDSF matrix was achieved using a pump perfusion system combined with agitation decellularization. The PDSF had a preserved intact vasculature, including a dominant vascular pedicle and its perforators. ("D-" indicates "decellularized" in this and other panels.) (C) A magnified view of the circled area in panel B shows artery and vein structures in the perforator bundle (the asterisk indicates a blood vessel). (D) Microfil-117 angiography confirmed that PDSF retained a patent vascular pedicle and microcirculatory vessels. (E) In a magnified view of the boxed area in panel D, polarized light microscopy shows that the perforators penetrated into muscle matrix. Each artery was accompanied by a vein branch. (F) A magnified view of the circled area in panel D shows Microfil-117 easily filling a patent small perforator. (G) DAPI staining revealed the absence of nuclear DNA in PDSF. (H) Nuclear DNA was significantly reduced in PDSF. *$P < 0.05$ vs. PNS. (I) GAG content was significantly decreased in PDSF. *$P < 0.05$ vs. PNS. (J) PDSF has strong mechanical properties. *$P < 0.05$ vs. native muscle and PDMM. The Student t-test was used for comparisons between 2 groups, as appropriate. ANOVA was used for comparisons among multiple groups, as appropriate. (K) SEM images show that the 3D porous, tubular, and nanofibrous architectures of the ECM were well preserved in PDSF.

PDSF was 2.39 ± 0.52 mm (n = 20). The results of the PicoGreen dsDNA assay revealed that the DNA content in the PDSF samples (0.032 ± 0.003 μg/mg dry weight) was significantly lower than that in the native tissue samples (1.38 ± 0.155 μg/mg dry weight; $P < 0.05$; n = 6 samples/group) (Fig. 1H). GAG content was also significantly lower in the PDSF samples (11.44 ± 1.90 μg/mg dry weight) than in the native tissue samples (44.03 ± 0.91 μg/mg dry weight; $P < 0.05$; n = 6 samples/group) (Fig. 1I). Uniaxial tensile testing showed that PDSF had high UTS (6.04 ± 0.5 MPa), elastic modulus (9.48 ± 2.16 MPa), and strain at failure (0.92 ± 0.3) (n = 6); these values were similar to those of native fascia and PDFM. Compared with PDMM, PDSF had significantly higher UTS and elastic modulus ($P < 0.05$) but similar strain at failure (Fig. 1J).

These data indicate that PDSF has strong mechanical properties. Such properties are particularly important for VML repair, which demands high tension and elastic recoil.

Microfil was easily injected into the flap matrix through the artery pedicle. Images of the injected Microfil revealed that the gastroepiploic artery and its branch remained intact after decellularization. The perforator bundle comprised 1 artery and 2 veins penetrating to the acellular muscularis layers, suggesting that the microcirculatory network was well preserved in the decellularized musculofascial layer (Fig. 1D–G). The length of the vascular pedicle was 5.5 ± 3.5 cm, with an artery diameter of 2.2 ± 1.5 mm and vein diameter of 2.8 ± 2.0 mm. These findings indicate that PDSF has well-maintained microcirculatory

vascularity and a dominant vascular pedicle. These elements provide the foundation for engineering ECM-based vascularized composite muscle flaps.

SEM findings were used to characterize the 3D architecture of PDSF (Fig. 1K). No cells were observed in the PDSF samples. Blood vessel structures were retained within the serosa and musculofascial layers. After adipose cells were removed from the loose connective tissues in the submucosa layer and smooth muscle cells were removed from the muscularis layer, nanofibrous structures were observed (fiber diameter $= 81.0 \pm 7.2$ nm, n = 10). The outer surface of the thin serosa layer had microridge structures (ridge height $= 3.8 \pm 0.2$ μm, n = 10). After the removal of the smooth muscle fibers, hollow and tubular structures were observed in the PDSF samples; these formations were characterized by a

layered-sheet structure (sheet-to-sheet distance $= 40.2 \pm 1.5$ μm, n = 10) and porous structure (pore size $= 74.8 \pm 3.4$ μm for smooth bundles and 19.5 ± 0.7 μm for single smooth muscle cells, n = 10). These data indicate that PDSF comprising 3 layers of muscle ECM and 1 layer of fascia ECM has a well-maintained ECM architecture that provides topographical cues for cell integration and that PDSF's porous and tubular structures with nanofibrous features resemble those of PDMM [32].

3.2. PDSF is free of allo- and xenoantigens

The presence and location of major ECM components in the PDSF scaffolds were assessed by IHC analysis. H&E staining and Masson
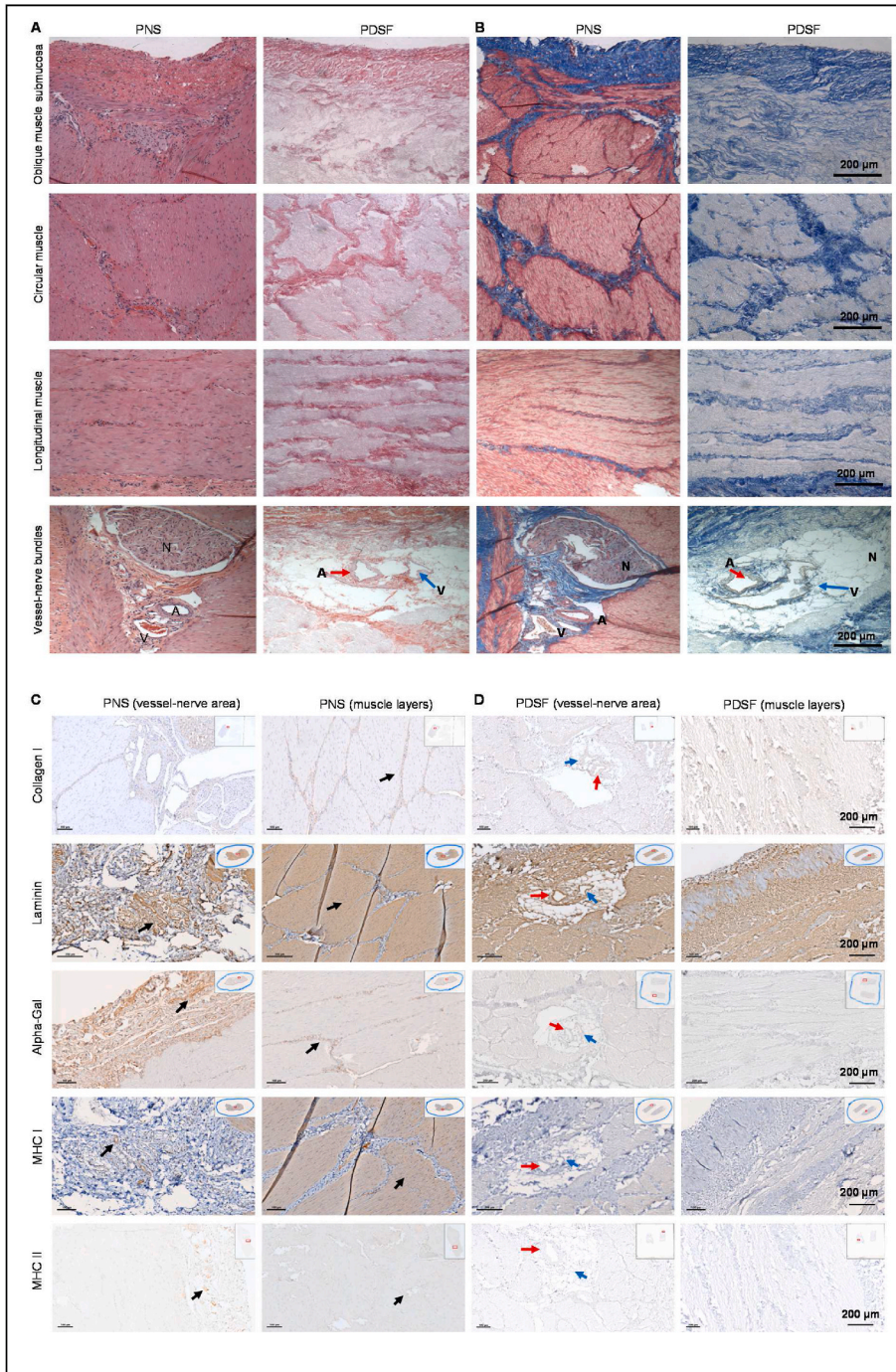

Fig. 2. IHC analysis of PDSF. (A&B) H&E staining (A) and Masson trichrome staining (B) of the cross-sections of all layers demonstrated that cell nuclei were present in native tissues (i.e., PNS) but absent in PDSF samples. PNS comprises a serosa layer (fascia) and 3 muscularis layers. These layers were well retained as composite collagen−based ECM in PDSF. Blood vessels and nerve structures in the serosa layer were also well maintained in PDSF. A, artery; V, vein; N, nerve. (C&D) In PNS (C), collagen I was strongly expressed in the vessel-nerve area and in stromal and epimysium tissue, whereas laminin was distributed richly in vessels, nerves, and muscle parenchymal structures. Similarly, in PDSF (D), corresponding structures showed strong expression of both collagen I and laminin. In PNS (C), α-gal was strongly expressed in vessel-nerve tissue located in the serosa fascia, connective tissue between muscle layers, and muscle epimysium; and whereas MHC I was expressed in most cells, MHC II was detected mainly in vessel-nerve structures. In PDSF (D), these 3 allo- and xenoantigens were absent. Inset images indicate the areas shown in the magnified views. Black arrows indicate the antigens of interest. Red arrows indicate arteries, and blue arrows indicate veins.

trichrome staining of the cross-sections of all layers demonstrated that cell nuclei were present in native tissues (i.e., PNS) but absent in the PDSF samples. The serosa (fascia layer) and 3 layers of composite musculofascial ECM were well maintained in the PDSF samples (Fig. 2A and B). Collagen I was detected around blood vessel structures (~32.0 ± 6.4% positive staining) and in the stroma and epimysium of muscle bundles (~12.7 ± 6.0% positive staining) in PNS and detected in corresponding locations (~4.7 ± 0.6% positive staining in vessel structures and ~29.2 ± 5.3% positive staining in muscle parenchyma) in PDSF (Fig. 2C and D). Laminin was highly expressed in both vessel-nerve (~12.7 ± 3.4% positive staining) and muscle parenchymal structures (~64.0 ± 6.9% positive staining) in PNS. Accordingly, after decellularization, muscle fibrous structures (~50.1 ± 5.4% positive staining) and blood vessel structures (~15.4 ± 1.8% positive staining) in PDSF were strongly positive for laminin (Fig. 2C and D), an important component of

the basement membrane necessary for cell attachment, adhesion, and integration. α-gal, which is absent in primates and humans and is recognized as the most potent xenoantigen, was enriched in the vessel-nerve areas (~19.2 ± 2.2% positive staining) and in the stromal tissue around the muscle fiber bundles (~17.8 ± 1.0% positive staining) in PNS. Whereas MHC II was predominantly expressed around the vessel-nerve structures (~15.7 ± 0.7% positive staining), MHC I, another strong antigen, was expressed in most PNS cells (~55.5 ± 5.6% positive staining in muscle parenchyma and ~5.1 ± 0.8% positive staining in vessel structures). These 3 major antigens, which provoke severe acute immunorejection in the recipient after transplantation, were absent in the PDSF samples (Fig. 2D). These histological data demonstrate that PDSF as a composite bioscaffold preserves native musculofascial ECM structures and lacks major antigenicity, making it safe for the clinical application of native-derived biologics.

Fig. 3. Proteomic profiling of PDSF. (A) Heatmap showing the fold changes in protein abundances in PDSF samples. (B) A Venn diagram of the numbers of proteins identified in PNS and PDSF. PDSF had significantly fewer proteins than PNS did. (C) A stacked bar graph shows the distribution of MS intensity among the matrisome subcategories for PNS and PDSF. (D) Quantitative analysis showed differences in the abundances of individual proteins in each matrisome and non-matrisome subcategory. Several proteins in both the matrisome and non-matrisome were enriched in PDSF. (E–I) GO functional classification in PDSF. (E) The most abundant and enriched proteins within the cellular component subset. (F) The network view of the cellular component subgroup grouped by function. The cutoff of the GO enrichment analysis was set to an adjusted *P*-value of 0.05. Enriched GO terms (those with a kappa score of ≥0.4) are depicted as nodes connected by lines that represent hierarchies and relationships among the terms. The node size reflects the significance of the term enrichment. Functionally similar terms are clustered together and are the same color. Only the names of the most significant terms within the clusters are shown. (G) The most abundant and enriched proteins within the biological process subgroup. (H) The network view of the biological process subgroup grouped by function. (I) The most abundant and enriched proteins within the molecular function subgroup. (J) A stacked bar graph shows the matrisome compositions by subcategory for PDSF, PDMM, and HDDM. (K) Quantitative analysis showed similar abundances of individual collagen proteins in the matrisomes of PDSF and PDMM. (For all panels, n = 3 biological replicates).
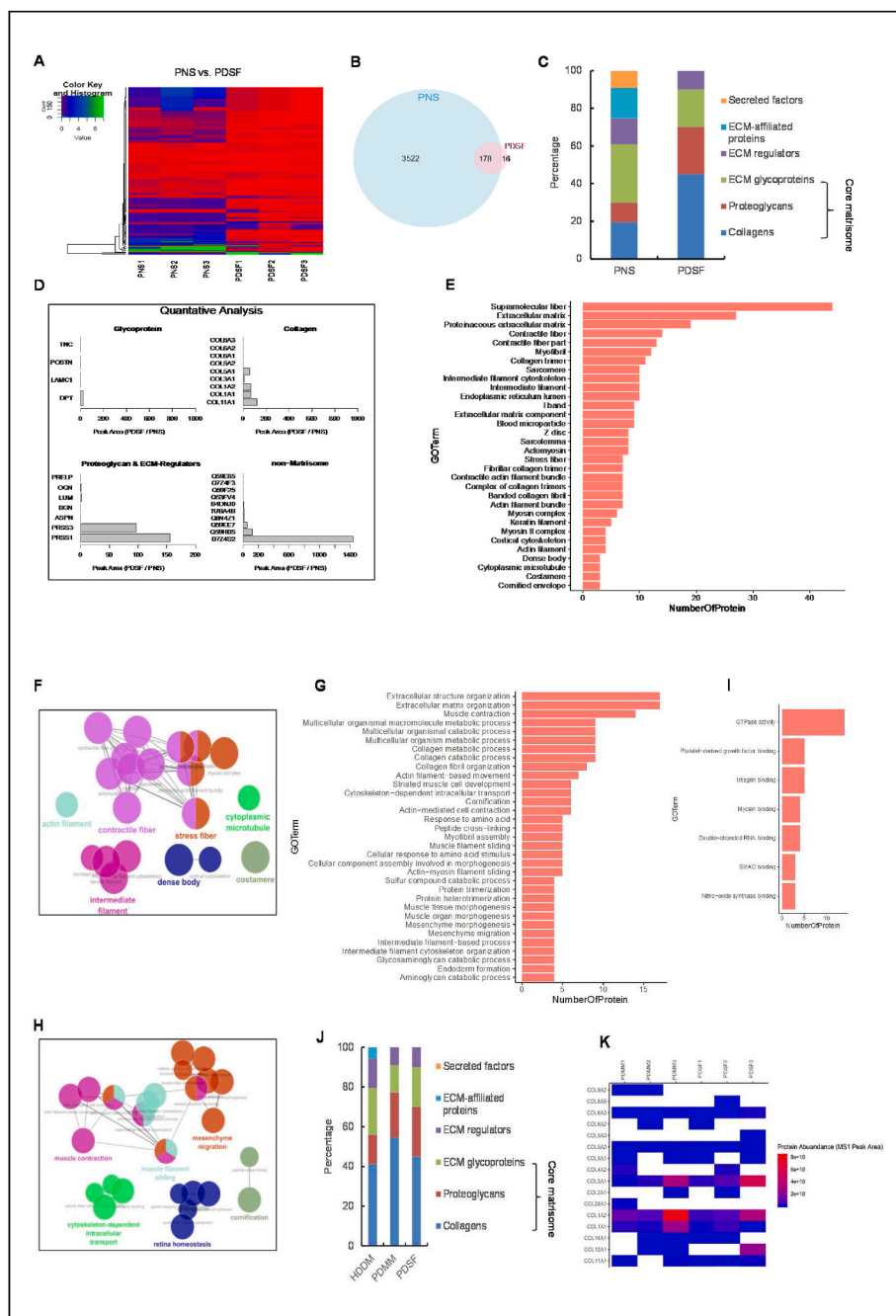
3.3. PDSF's matrisome proteins are highly similar to those in the core matrisome of skeletal muscle

We used LC-MS/MS for the in-depth characterization of the proteomic profile of PDSF. For each group, triplicate runs yielded consistent results. R scripts were used to generate the heatmap analysis of PNS vs. PDSF. The identified proteins were expressed strongly in the PNS groups, but the majority of these proteins had significantly decreased abundance in the PDSF groups (Fig. 3A and B). A total of 194 proteins in PDSF were classified as matrisome or non-matrisome proteins according to the classification rules of the MIT Matrisome Project. We identified 20 matrisome proteins, including collagens, glycoproteins, proteoglycans, and ECM regulators (Table S1). We identified 9 collagen proteins, including fibrillary collagens IA1, IA2, IIIA1, VA1, and VA2, which contribute to tensile strength. In particular, collagen V has been found to augment tissue generation and organoid formation [35], and collagen XIA1 helps maintain the spacing and width of the network-forming collagens VIA1, VIA2, and VIA3. Collagen VI, which is primarily associated with the skeletal muscle ECM, maintains regularity in muscle function and stabilizes the cell membrane [36]; it has also been shown to benefit mesenchymal cell growth and inhibit apoptosis [37]. These special functions make collagen VI an important component of any bioscaffold used for muscle tissue engineering and reconstruction.

In addition, we identified several ECM glycoproteins, including dermatopontin, which interacts with decorin and modifies collagen fibrillogenesis; laminin γ, which is the major noncollagenous constituent of basement membrane and has been implicated in a wide variety of biological processes [38]; periostin; and tenascin C, which has been found to enhance cell proliferation and migration and ultimately improve regenerated tissue morphology [39]. Several proteoglycans and ECM regulators were also observed (Fig. 3C and D). Some matrisome proteins, such as ECM-affiliated proteins and secreted factors, were significantly depleted in PDSF compared with PNS. However, the "core matrisome," which is key to the overall bioscaffold structure and facilitates cell seeding and integration, was well preserved in PDSF, as indicated by PDSF's retention of collagens, glycoproteins, and proteoglycans (Fig. 3C). Among these core matrisome components, several proteins were significantly enriched in PDSF, including collagens XIA1, IA1, IA2, IIIA1, and VA1; the glycoprotein dermatopontin; the proteoglycan lumican; and the ECM regulators PRSS1 and PRSS3 (Fig. 3D).

Conversely, a total of 174 non-matrisome, or cellular, proteins were identified in PDSF (Table S1). Although PDSF had high numbers of remnant cellular proteins, its abundance of these proteins was significantly decreased compared with PNS (Fig. 3A). PDSF had 10 well-retained cellular proteins, including B7Z4S2, which is cDNA FLJ51252, highly similar to collagen α-1(I) chain; Q59HB5, which is α 1 type XI collagen isoform C preproprotein variant; Q59EE7, which is pro-α-1 type V collagen variant; and TUBA4B, which is putative tubulin-like protein α-4B (Fig. 3D). These cellular proteins are all related to collagen matrix (awbs://www.uniprot.org/). Our results are consistent with those reported for other acellular scaffolds [40]. For example, 58 matrisome proteins and 459 cellular proteins were identified in a rat decellularized liver scaffold [41]. Porcine acellular vocal fold mucosa also contains a large number of non-matrisome proteins [42]. In a rat decellularized pancreas scaffold, 526 proteins were identified, including 133 extracellular proteins and 393 intracellular proteins [35]. The detection of remnant cellular proteins underscores the challenge of removing all cellular materials from organ and flap tissues; however, perfusion decellularization is a powerful technique for depleting nucleic acids and retaining important ECM structures [41,43]. Remnant cellular proteins do not negatively impact ECM-based tissue engineering [35, 42]. However, the role of these proteins in the subsequent host reaction and remodeling process *in vivo* needs to be elucidated [41].

Gene Ontology (GO) functional classification according to the terms "cellular component," "biological process," and "molecular function" was performed to identify the functions of each component of PDSF. The cellular component mostly included supramolecular fibers, ECM, and skeleton filaments, which have highly abundant proteins (Fig. 3E and F). The biological processes were mostly related to ECM organization, extracellular structure organization, muscle contraction, collagen metabolism, and muscle tissue morphogenesis (Fig. 3G and H). Moreover, the molecular functions were mainly ECM-related processes such as integrin binding, myosin binding, growth factor binding, and GTPase activity (Fig. 3I). These data indicate that matrisome proteins in PDSF are major contributors to the enrichment of GO terms that are highly related to muscle physiological functions that could promote cell repopulation and muscle regeneration *in vitro* and *in vivo*.

To better define the molecular cues of PDSF, we compared PDSF with HDDM, which has been widely used in reconstructive surgeries such as abdominal wall reconstruction and breast revision, as well as with PDMM, which is the gold-standard bioscaffold for skeletal muscle tissue engineering [25,32]. In HDDM, 365 proteins were identified, including 34 matrisome proteins and 331 non-matrisome proteins. In PDMM, 283 proteins were identified, including 22 matrisome proteins and 261 non-matrisome proteins. Among these proteins, 105 were shared between PDSF and PDMM, and 92 were shared among all 3 scaffolds. HDDM had the most cellular proteins, whereas PDSF had fewer cellular proteins than PDMM and HDDM did. PDSF and PDMM not only had similar numbers of matrisome proteins (20 vs. 22; among these, 16 were shared) but also had similar abundances of core matrisome proteins such as collagens (11A1, 1A1, 1A2, 3A1, 5A1, 5A2, 6A1, 6A2, and 6A3), glycoproteins (dermatopontin), and proteoglycans (biglycan, lumican, osteoglycin, and prolargin) (Fig. 3J and K). HDDM and PDMM shared only 105 proteins; in addition, HDDM and PDMM had less similarity in terms of both matrisome protein terms and abundance (Fig. 3J). These data indicate that the matrisome of PDSF highly resembles that of PDMM (Fig. 3K). In using PDSF to engineer muscle tissue, it would be particularly meaningful to have the muscle matrisome's "zip-codes," which would direct or support site-appropriate cell attachment and differentiation [44]. The differences in the core matrisomes of HDDM and PDMM indicate that skin-derived ECM is not an ideal bioscaffold for driving muscle cell differentiation and proliferation. This could explain the small amount of muscle regeneration that results from using HDDM for hernia repair in experimental animal and clinical studies [34,45–47].

3.4. PDSF supports hASCs' proliferation, alignment, and differentiation

Owing to their adult stem cell characteristics and easy isolation with conventional liposuction procedures, hASCs are the predominant cell source for tissue engineering [48]. hASCs are capable of asymmetrical reproduction, i.e., simultaneous self-renewal and differentiation. We assessed the interaction between hASCs and PDSF, particularly in terms of hASCs' proliferation and differentiation. One day after plating, hASCs were well attached to PDSF on either the serosa side or the muscularis side (Fig. 4A). Cell viability assays demonstrated that hASCs continued to proliferate thereafter: hASCs on the serosa side proliferated from day 1 (113 ± 4 cells/mm^2) to day 7 (439 ± 10 cells/mm^2) with a doubling time of 36.8 h, and hASCs on the muscularis side proliferated from day 1 (105 ± 6 cells/mm^2) to day 7 (426 ± 18 cells/mm^2) with a doubling time of 35.7 h ($n = 3$) (Fig. 4A). hASCs elongated and formed aligned patterns from day 1 to day 7 in culture on PDSF (Fig. 4A and B). For example, after 7 days, 88% of the hASCs cultured on the serosa side oriented along the x-axis at an angle of less than 10°, while 72% of the hASCs cultured on the muscularis side oriented along the y-axis at angles ranging from 80 to 90°. In contrast, the hASCs cultured on 2D glass slides were randomly oriented at angles ranging from 0 to 90° (Fig. 4C).

One of the important functions of hASCs is their differentiation capability. PDSF extraction significantly induced hASCs' adipogenesis and osteogenesis (Fig. 4D–H). Lipid droplets were observed in the peripheral area on day 3 in the experimental group but were observed in fewer areas on day 6 in the control groups (Fig. 4D,E,G). Similarly, PDSF-CDM significantly increased osteoblasts' differentiation and
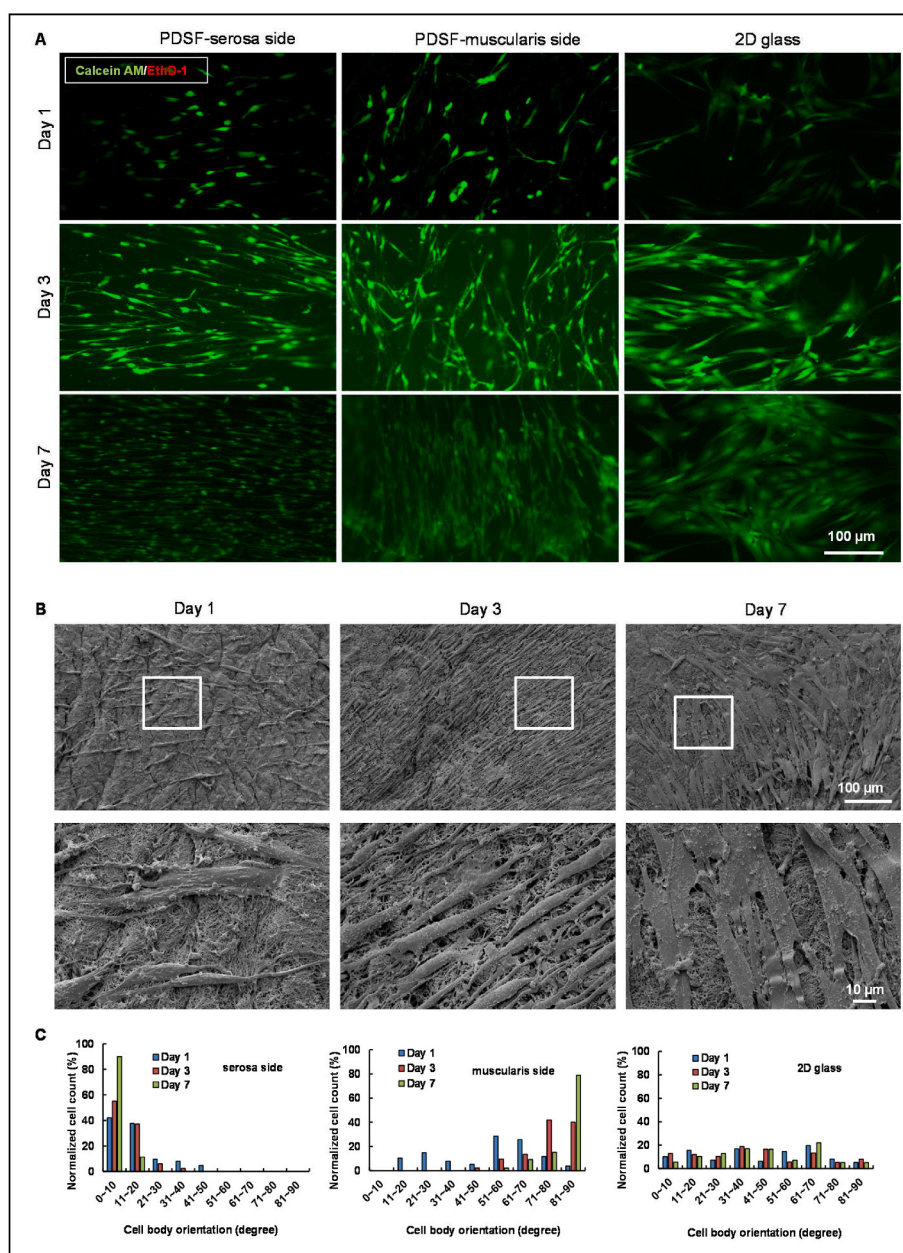
Fig. 4. hASCs integrate with PDSF. (A) Confocal microscopy images show hASC growth on PDSF and 2D glass. Cells were stained with calcein AM (green) and ethidium homodimer-1 (red) 1, 3, and 7 days after seeding. (B) SEM images show hASC proliferation on PDSF from day 1 to day 7. The white boxes indicate the areas shown in the high-magnification images. (C) Cell body orientation reflected an alignment pattern of hASC growth on both the serosa and muscularis sides of PDSF. (D) A differentiation assay showed that PDSF extraction−conditioned medium significantly induced hASC adipogenesis and osteogenesis. (D&E) Oil-Red-O staining. Lipid droplets occurred in the peripheral area on day 3 (D) in the experimental group but occurred in fewer areas on day 6 (E) in the control group. (F) Alizarin-Red-S staining. Significantly more calcium deposition was observed in the experimental group than in the control group on day 10. (G) Differences in adipocyte differentiation between CDM and DM. *$P < 0.05$. (H) Differences in osteogenesis between CDM and DM. *$P < 0.05$. The Student t-test was used for comparisons between 2 groups, as appropriate. ANOVA was used for comparisons among multiple groups, as appropriate.

function, as evidenced by the greater calcium deposition in CDM compared with that in regular DM (Fig. 4F,H). These data indicate that PDSF provides a healthy microenvironment favorable to hASCs' stemness. Future studies with LC-MS/MS could help identify the specific molecules in PDSF that improve stem cell differentiation.

3.5. PDSF-hASC synergy skews monocytes towards M2 macrophage polarization

Bioscaffold implantation often activates a foreign body response.

Among host immune cells, macrophages play an important role in determining the outcomes of ECM-based implants. Macrophages have pro-inflammatory M1 or anti-inflammatory M2 polarization. Hence, we determined whether the PDSF-hASC culture system can modulate macrophage phenotypes. Cell culture inserts were used to achieve indirect contact between hASCs and CD14$^+$ macrophages (M0 macrophages) in a coculture system (Fig. 5A). Flow cytometry and biological assays were used to assess changes in the macrophages during coculture. On day 7, compared with the control group (group 1), groups 2, 3, and 4 had significantly more CD206+ M2 macrophages (22.0% ± 0.7% vs.
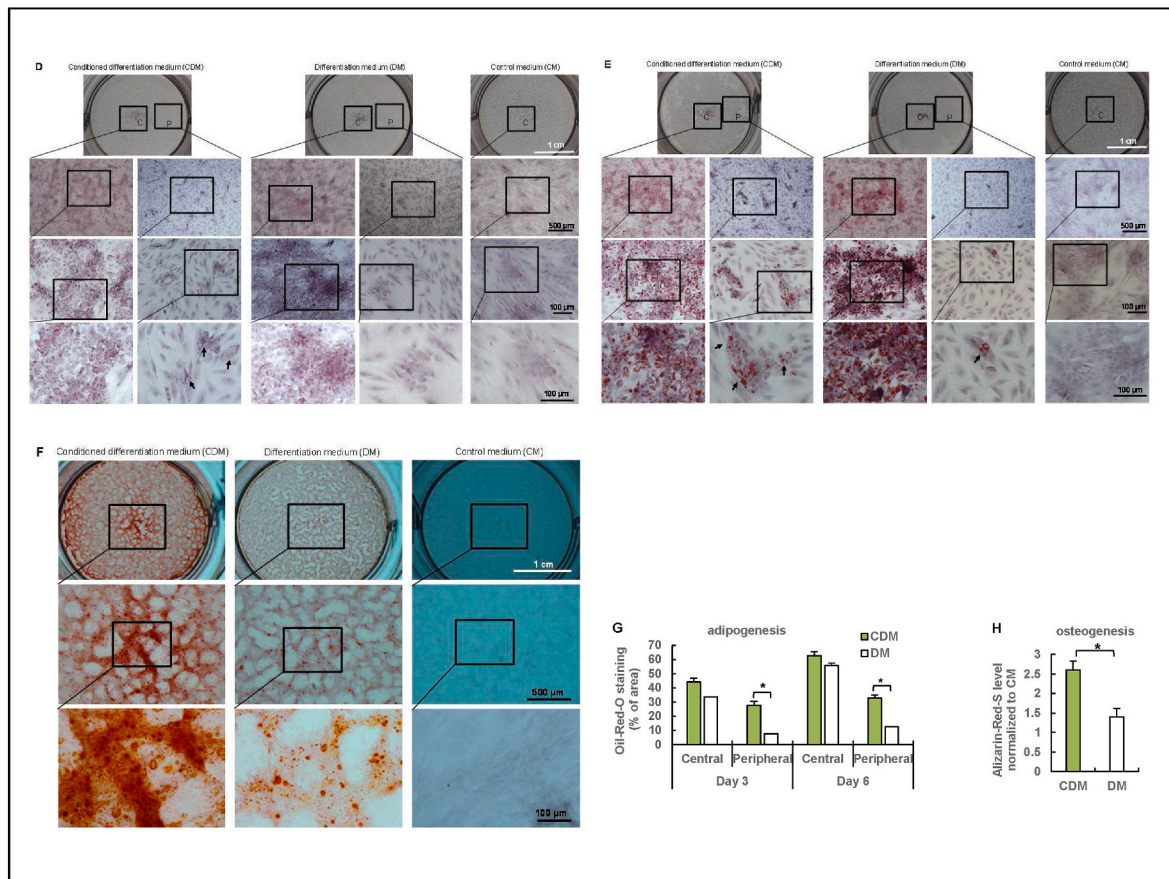
Fig. 4. (*continued*).

42.1% ± 3.4%, 79.2% ± 1.4%, and 90.5% ± 0.5%, respectively; $P <$ 0.05). All groups had substantially fewer CD16$^+$ M1 macrophages after 7 days of culture. Whereas human leukocyte antigen DR (HLA-DR) was highly expressed in most of the cells in groups 1, 2, and 3, hASCs combined with PDSF in group 4 had significantly decreased levels of HLA-DR expression. On day 7, group 4 had significantly more CD206+/ HLA-DR− cells than groups 1, 2, and 3 did (39.9% ± 1.6% vs. 7.3% ± 1.9%, 0.26% ± 0.06%, and 0.70% ± 0.25%, respectively; $P <$ 0.05). These data indicate that either PDSF or hASCs favor M2 macrophage polarization in the coculture system and that the combination of hASCs and PDSF especially favors this polarization (Fig. 5A–G).

The cytokine measurements from the Bio-Plex immunoassay coincided with the flow cytometry findings. The cytokine IL-10, a biomarker of M2 macrophages, was significantly increased in the medium of groups 3 and 4, especially on day 3. Although M2 macrophages' secretion of IL-10 decreased from day 3 to day 7, it remained at detectable levels compared with those in group 1 at day 5 and day 7 (Fig. 5H). VEGF, an angiogenesis factor, significantly increased from day 3 to day 7 in group 3 and particularly in group 4 (Fig. 5I). None of the groups showed significant secretion of IL-2, IL-4, IL-8, IFN-γ, or TNF-α, the proinflammatory cytokines associated with M1 macrophages. In addition, higher levels of IL-6 were detected in the medium of group 4 from day 3 to day 7 and in that of group 3 at day 7 (Fig. 5J).

To identify the origin of IL-6, we cultured hASCs with or without other cell types, such as HSMMs and HUVECs, on both 2D glass and 3D PDSF. In most conditions, but especially in 3D PDSF, hASCs constitutively produced higher levels of IL-6 (Fig. 5K–M). Because group 1 did not have IL-6 and group 2 had only very low levels of the cytokine, hASCs were likely the predominant source of IL-6 in the coculture system. Because M1 macrophages usually secrete high levels of IL-6, our data indicate that hASC-derived IL-6 has a role in a negative feedback

loop that skews CD14$^+$ M0 monocytes towards IL-10−producing, anti-inflammatory M2 macrophages. These findings are consistent with previous reports about the immunomodulatory mechanisms of other types of mesenchymal stromal stem cells, such as bone marrow-derived mesenchymal stem cells (BM-MSCs) [49]. That hASCs have immunomodulatory properties associated with constitutive IL-6 production when they are cultured with HSMMs and/or HUVECs on PDSF has important implications for using the PDSF-hASC construct for muscle tissue engineering.

We also examined 41 human growth factors in the culture medium. Six of these growth factors were detected at relatively high levels. Again, VEGF was present in only groups 3 and 4, but it was significantly elevated in these groups. IGFBP-6 was elevated in group 4. Transforming growth factor β (TGF-β), epidermal growth factor (EGF), and granulocyte-macrophage colony-stimulating factor were increased in groups 3 and 4, although their levels did not differ significantly between the groups (Fig. 5N and O). Next, an aortic ring assay was used to further test the biological activity of growth factors produced by the PDSF-hASCs culture system. The medium from groups 3 and 4 significantly induced the outgrowth of endothelial cells and smooth muscle cells from the aortic ring (Fig. 5P). Both cell types formed microvessel-like branches inside and outside the ring in 3D collagen gel. Two-photon excitation microscopy showed that the vascular network augmented by the group 4 medium was distinct from those augmented by the other groups' media (Fig. 5Q–U).

Taken together, the above *in vitro* data suggest that seeding hASCs on PDSF enhances the cells' paracrine activity, which in turn mediates angiogenesis and immunomodulation: hASCs promote angiogenesis by secreting growth factors such as VEGF, and they modulate inflammatory immune responses by producing IL-6 to switch monocytes towards the M2 phenotype (Fig. 5V). These important functions could drive
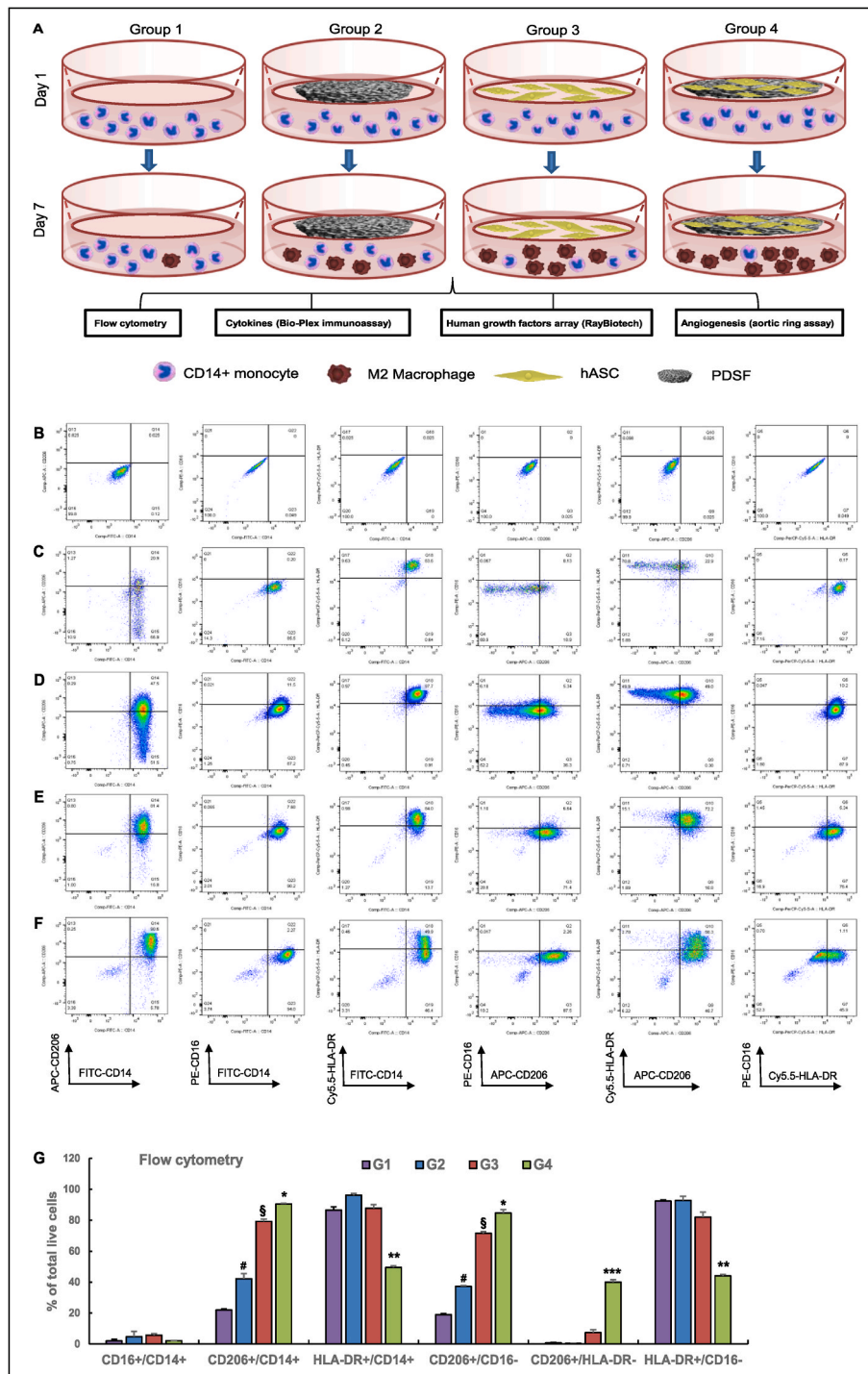
Fig. 5. PDSF-hASC synergy induces monocytes towards M2 macrophage polarization. (A) The experimental design of the indirect co-culturing of monocytes and hASCs *in vitro* (n = 3 replicates). (B–F) Representative flow cytometry dot plots of monocytes allowed to differentiate for 7 days in the presence of various conditions: B shows the isotype control; C, group 1 (G1); D, group 2 (G2); E, group 3 (G3); and F, group 4 (G4). (G) Rates of CD14, CD16, CD206, and HILA-DR expression among day 7 monocytes differentiated under various conditions. *$P < 0.05$ vs. G1 and G2; **$P < 0.05$ vs. G1, G2, and G3; ***$P < 0.01$ vs. G1, G2, and G3; §$P < 0.05$ vs. G1 and G2; #$P < 0.05$ vs. G1. (H) IL-10 secretion in fresh medium following coculture. §$P < 0.01$ vs. G1 and G2 on day 3; *$P < 0.05$ vs. G3 on day 3; #$P < 0.05$ vs. G2, G3, and G4 on day 7. (I) VEGF secretion in collected fresh medium following coculture. *$P < 0.05$ vs. G1, G2, and G3 at the same time point; §$P < 0.05$ vs. G1 and G2 at the same time point. (J) IL-6 secretion in fresh medium following coculture. *$P < 0.05$ vs. G1, G2, and G3 at same time point; §$P < 0.05$ vs. G1 and G2 on day 7. (K–M) IL-6 secretion in collected fresh medium following various culture conditions. *$P < 0.05$ vs. the control group at the same time point; §$P < 0.05$ vs. the same group on day 5 and day 7. (N) Representative film of the human growth factor array. Six growth factors were detected in collected fresh medium on day 7. (O) Densitometry analysis of growth factor expression. G3 and G4 had significantly higher expression of both VEGF and IGFBP. *$P < 0.05$ vs. G1, G2, and G3; §$P < 0.05$ vs. G1 and G2. (P) Representative phase-contrast images of aortic rings cultured with various conditioned media on day 7. The G4-conditioned medium resulted in significant vessel outgrowth from the aortic ring. (Q) Light microscopy image of microvessel outgrowth (black arrows) from the aortic ring (asterisk) of G4. (R&S) For G4, 2-photon excitation microscopy revealed the outgrowth of CD31^{+} endothelial cells (green) and SMA + smooth muscle cells (red) from the aortic ring (asterisk), which formed a microvascular network (white arrows) both outside the ring (R) and inside the ring (S). (T) A large vessel outgrowth (white arrow) from the aortic ring (asterisk) of G4. The scale bars on the x-ases in R-T are 50 μm. (U) Aortic ring microvessel density measured on day 7. *$P < 0.05$ vs. G1, G2, and

G3; #$P < 0.05$ vs. G1 and G2. The Student t-test was used for comparisons between 2 groups, as appropriate. ANOVA was used for comparisons among multiple groups, as appropriate. (V) A hypothetical model of hASC-induced M2 polarization. PDSF integration activates hASCs to constitutively produce IL-6, which skews CD14$^+$ M0 monocytes towards anti-inflammatory, IL-10–producing M2 macrophages via a negative feedback mechanism. In turn, PDSF-hASC synergy has anti-inflammatory, immunomodulatory, and angiogenic properties that are initiated by and dependent on hASCs' secretion of soluble factors such as IL-6, VEGF, and IGF.
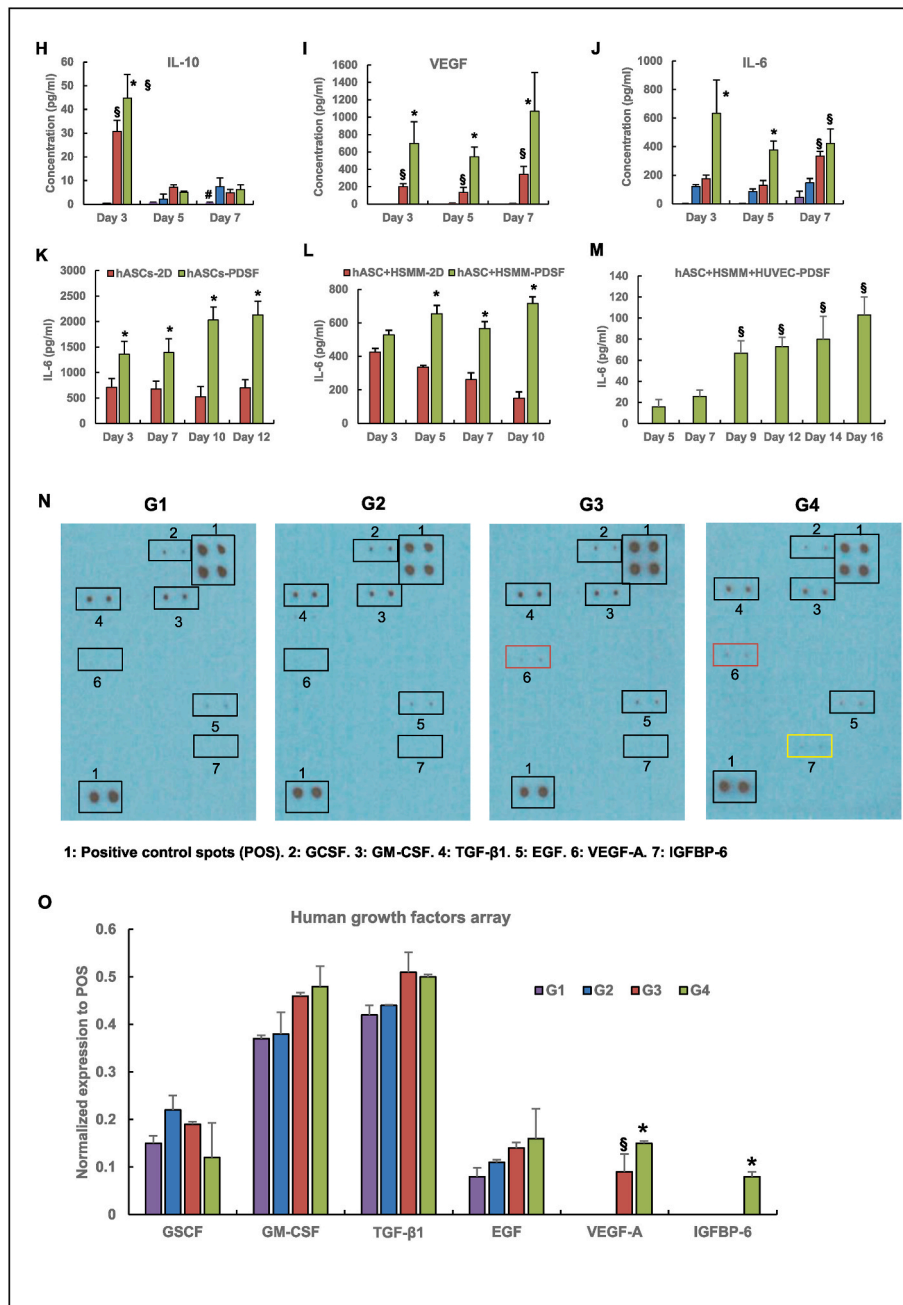

1: Positive control spots (POS). 2: GCSF. 3: GM-CSF. 4: TGF-β1. 5: EGF. 6: VEGF-A. 7: IGFBP-6

Fig. 5. (*continued*).

3.6. PDSF-hASC synergy improves the interconnection and communication of HSMMs and HUVECs

We investigated whether PDSF supports the integration of skeletal muscle cells and endothelial cells. Two-photon excitation microscopy showed that desmin + HSMMs cultured on PDSF were well attached, grew, and formed an alignment pattern; this pattern was absent when HSMMs were cultured on 2D glass or 3D collagen gel (Fig. 6A). HSMMs

constructive remodeling and promote neovascularization and hence provide a strong rationale for using PDSF-hASC constructs for muscle tissue engineering.

and HUVECs cocultured on PDSF grew well compared with those cocultured on 2D glass or collagen gel, and HSMMs cultured on PDSF formed bundles of aligned cells. However, CD31$^+$ HUVECs did not form vessel-like networks on any of the 3 surfaces (Fig. 6B). HUVECs aggregated as vascular structures in the presence of hASCs on 2D glass (Fig. S2). Therefore, HSMMs and HUVECs were cultured together with hASCs on PDSF. In this triculture condition, HSMMs demonstrated alignment, and HUVECs communicated with each other to form vessel-like networks within HSMM bundles. With the exception of HSMM alignment, similar phenomena occurred on 2D glass and collagen gel (Fig. 6C, Supplementary Video 1). Imaging analysis revealed that, in the PDSF culture condition, HSMMs, either alone or with other cells, had
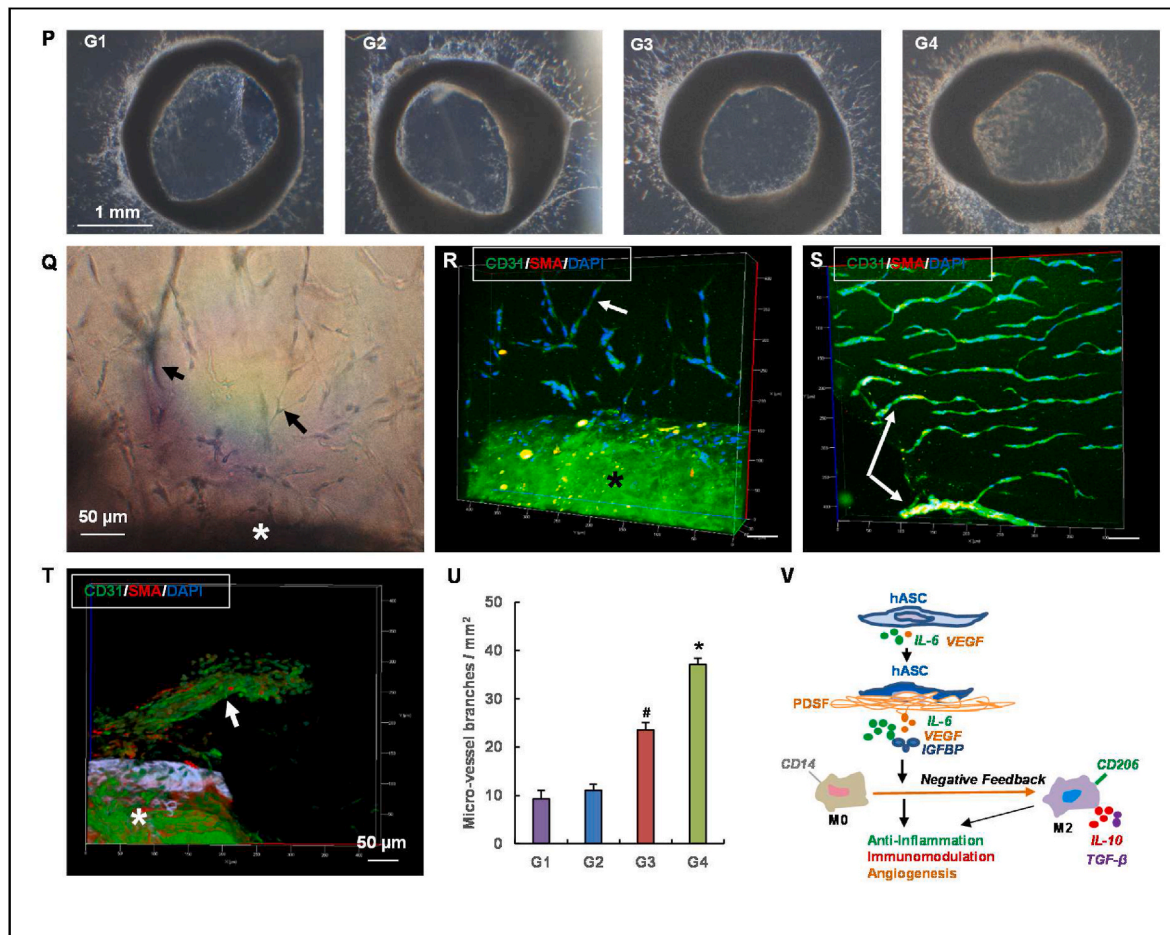
Fig. 5. (continued).

significantly increased numbers (as defined by the area of their red fluorescence), cell length and alignment (defined by cell body orientation), and interconnection (defined by dendrite body area, an overall parameter used to describe the fiber branches and communication between HSMMs) (Fig. 6D–I). HUVECs formed significant vascular-like networks in all static culture conditions, but only in the presence of hASCs. These data indicate that PDSF could provide an ideal niche for the repopulation and proliferation of both endothelial cells and skeletal muscle cells and that PDSF-hASC synergy improves the interconnection of HSMMs and HUVECs to form muscle-vessel bundles. hASCs likely mediate intercellular interactions between HSMMs and HUVECs via the paracrine action of growth factors such as VEGF.

Supplementary data related to this article can be found online at https://doi.org/10.1016/j.bioactmat.2022.10.023

3.7. The perfusion coculture approach augments PDSF prevascularization

Complete prevascularization and endothelialization are key to successful flap engineering. Therefore, we used a dynamic perfusion culture protocol to investigate PDSF prevascularization. When HUVECs were cocultured with hASCs on PDSF scaffolds, cells aggregated, capillary-like structures formed, and interconnected branches developed within 1 week (Supplementary Video 2). Aided by the perfusion culture approach, the vascular tree became bigger, denser, and more complex and mature along re-endothelialized perforators by week 2 and week 3 (Fig. 7A–C, Supplementary Video 3&4). Coculturing hASCs and HUVECs resulted in a partially re-endothelialized main vascular pedicle by week 3 (Fig. 7D). Imaging analysis confirmed that the total area and volume of the vessel networks significantly increased with culture time in the PDSF

parenchyma (Fig. 7E–G) and main pedicle (Fig. 7H&I). These data suggest that a perfusion coculture approach, aided by the PDSF vasculature, can achieve mature prevascularization. Prevascularized PDSF could be easily anastomosed and integrated with the host circulatory system, thus reducing the ischemia duration and increasing flap survival and improving reconstructive outcomes.

Supplementary data related to this article can be found online at https://doi.org/10.1016/j.bioactmat.2022.10.023

3.8. PDSF has immunomodulatory properties

The xenotransplantation of PDSF into Fischer 344 rats was evaluated at 2 weeks (Fig. 8A) and 4 weeks (Fig. 8B). H&E staining and Masson trichrome staining showed that despite cellular and vascular infiltration in the graft, the vast majority of the explant was collagenous connective tissue. There was a thin fibrosis capsule around the graft. MyoD1+ cells were detected within the graft, with more distributed in the peripheral area than in the central area. Both CD163+ M2 macrophages and CD80+ M1 macrophages were found throughout the section. Tissue section analysis showed that M2 was the dominant macrophage phenotype; the overall M2:M1 ratio was 4.97 ± 0.93 at 2 weeks and 1.90 ± 0.28 at 4 weeks (Fig. 8C). The tendency of M2 macrophages to replace M1 macrophages from the peripheral area towards the central area was attributed to the gradual neovascularization of the graft from the outside in. PDSF remodeling started at the outside layers, where degraded peptides would activate macrophage polarization [7].

Besides macrophages, a few CD3+ T cells were observed in the tissue. Among these cells, abundant FoxP3+ regulatory T cells (T-regs) were predominant (Fig. 8). T-regs play an important role in inhibiting the
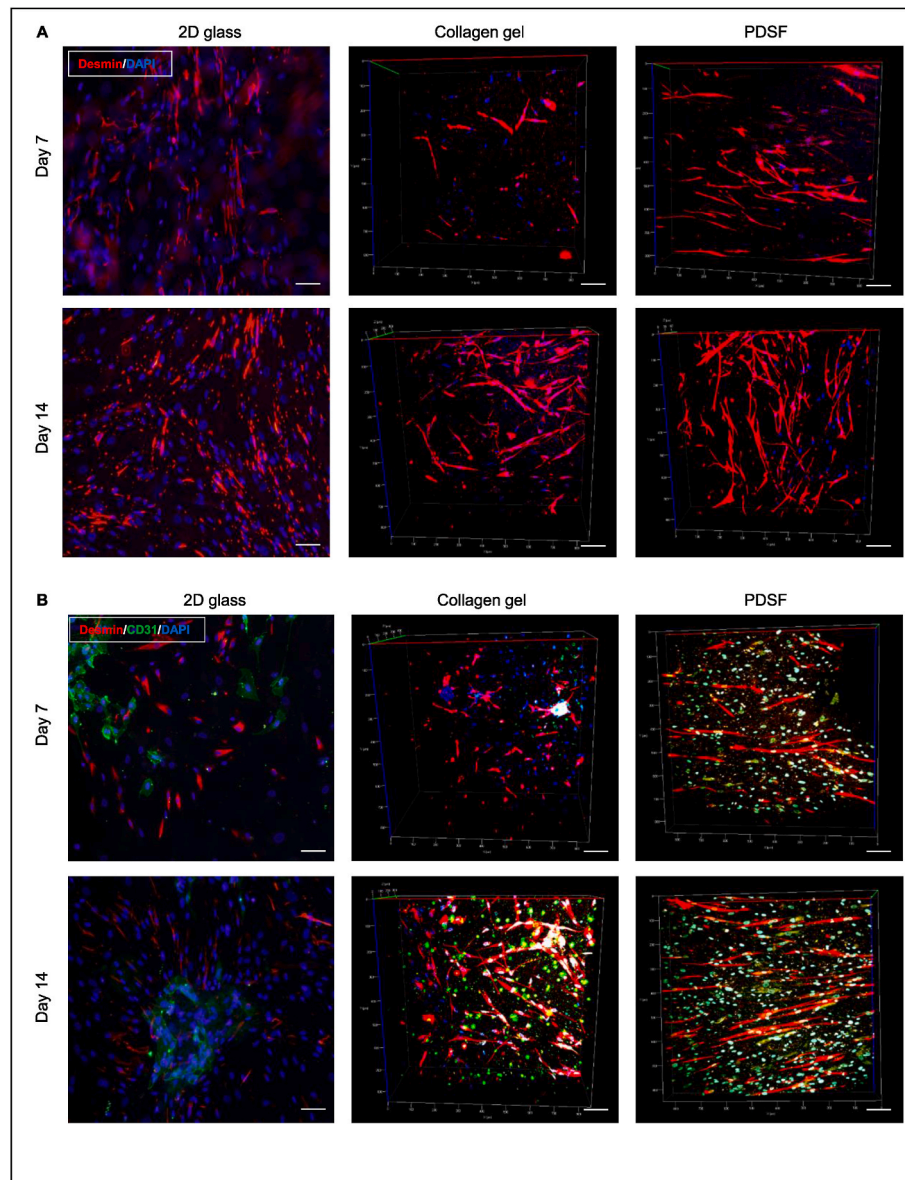
Fig. 6. PDSF-hASC constructs support the interconnection and proliferation of HSMMs and HUVECs. (A) Two-photon excitation microscopy reveals that HSMMs (red) grew well on 2D glass, collagen gel, and PDSF but that these cells elongated and formed clear alignment patterns on only PDSF. (B) Cocultures of HSMMs and HUVECs on 2D glass, collagen gel, and PDSF. Both cell types grew well; however, HUVECs (green) did not form vessel-like networks on all surfaces, and HSMMs (red) branched and aligned on only PDSF. (C) Tricultures of hASCs, HSMMs, and HUVECs on 2D glass, collagen gel, and PDSF. With hASCs present, HUVECs (green) formed vessel networks on all surfaces. On PDSF in particular, HUVECs formed vascular-like networks entangled with elongated and aligned HSMMs (red) by day 14. The scale bars on the x-ases in A-C are 50 μm. (D–I) Image analysis revealed that HSMMs—alone or in co- or triculture conditions—proliferated on PDSF, as evidenced by cell numbers (D), cell length (F), dendritic body formations (G), and cell body alignment (H&I). Moreover, HUVEC growth on all 3 surfaces was significantly increased in the triculture condition (E). (D: *$P < 0.05$ vs. the same surface on day 7 and 2D glass on day 14 within the same culture condition; #$P < 0.05$ vs. the same surface on day 7 and 2D glass and collagen gel on day 14 within the triculture condition. F&G: *$P < 0.05$ vs. 2D glass and collagen gel at the same time point within the same culture condition. E: *$P < 0.05$ vs. the same surface on day 14 within the coculture conditions and day 7 within the triculture condition. The Student t-test was used for comparisons between 2 groups, as appropriate. ANOVA was used for comparisons among multiple groups, as appropriate.

activation of T cells and inducing their apoptosis to promote immuno-suppression. A previous study demonstrated that decellularized skeletal muscle scaffolds display highly desirable immunomodulatory effects that skew the host response toward M2 macrophages, Th2 T cells, and cytokine profiles [50]. In agreement with that study, our data suggest that PDSF's immunomodulatory properties are characterized by resident M2 macrophages and that the predominance of T-regs, which indicated scaffold acceptance following implantation, further resulted in the regeneration of MyoD1+ myogenic cells. The localization of muscle cells was highly related to the distribution of specific macrophage subtypes;

more myogenesis occurred in areas that had both neovascularization and more M2 macrophages. Although remodeling was still occurring at 4 weeks, especially in the center of the PDSF graft, few chronic granu-loma or giant cells were detected throughout the graft.

The pathobiological characteristics of PDSF xenotransplantation closely resembled those of the implantation of RNM and RNS from Fischer rats into syngeneic recipients in terms of inflammatory and immune cell infiltration and distribution. However, compared with PDSF, RNM, and RNS, fresh xenografts from pig skeletal muscle (PNM) and stomach muscle (PNS) stimulated strong immunorejection
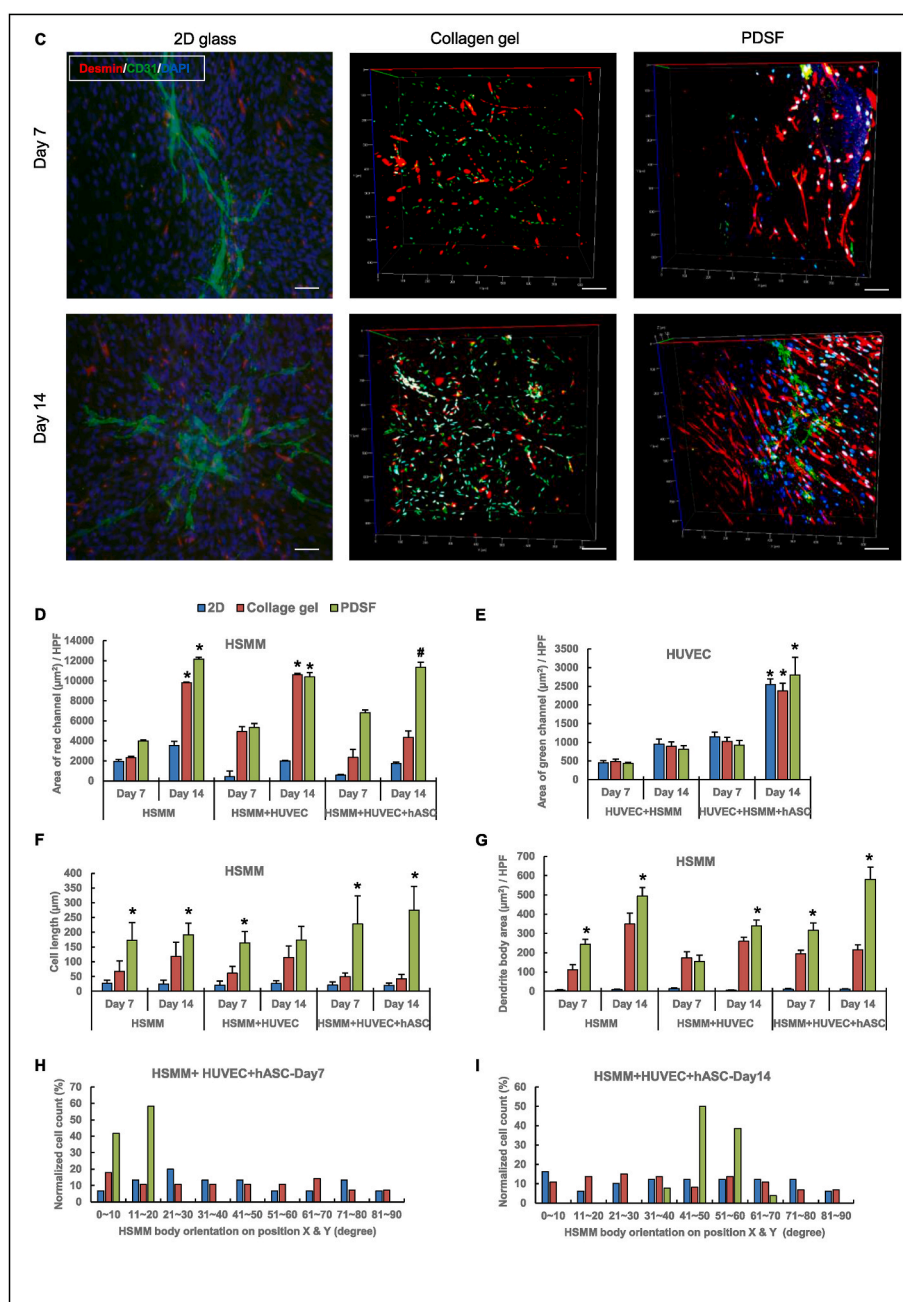
Fig. 6. (continued).

postoperatively, as evidenced by severe inflammation characterized by significant CD80$^+$ macrophage and CD3$^+$ T-cell infiltration, which caused the graft to lose structure and disintegrate (Fig. 8). Further investigations are required to identify the PDSF protein components that are the true specific antigens/immunomodulators that stimulate specific cell subsets and to elucidate the mechanisms underlying these interactions. Long-term observation of the xenograft *in vivo* would provide a more complete picture of the characteristics of foreign body reaction to PDSF and help determine the significance of such findings [50].

3.9. VML can be successfully reconstructed with prevascularized PDSF in vivo

The use of PDSF for VML reconstruction was assessed using a nude rat full-thickness abdominal wall defect model. After VML repair with PDSF or prevascularized PDSF, no infection or wound dehiscence was observed, and no hernia occurred. All grafts appeared to be completely integrated with surrounding tissues (Fig. 9A–D). Graft implantation for abdominal wall repair did not cause any organ or bowel adhesion and resulted in only very small and weak omentum adhesion (adhesion scale of PDSF vs. prevascularized PDSF: 1.3 ± 0.3 vs. 1.0 ± 0.2 at 1 month, P > 0.05; 0.9 ± 0.4 vs. 1.1 ± 0.5 at 3 months, P > 0.05). Mechanical tests showed that the tissue-graft interface had strong mechanical properties at 1 month and 3 months postoperatively. The mechanical properties of the PDSF and prevascularized PDSF implants did not differ significantly (PDSF vs. prevascularized PDSF at 3 months: UTS, 5.5 ± 2.4 MPa vs. 6.6 ± 2.1 MPa; elastic modulus, 21.6 ± 10.9 MPa vs. 21.4 ± 2.3 MPa; strain at failure, 0.47 ± 0.08 vs. 0.55 ± 0.07). However, the elastic modulus at the interface increased substantially from 1 month to 3 months in both the PDSF group (11.0 ± 2.5 MPa vs. 21.6 ± 1.09 MPa) and the prevascularized PDSF group (9.5 ± 2.4 MPa vs. 21.4 ± 2.3 MPa). These data suggest that both scaffolds healed and integrated with surrounding
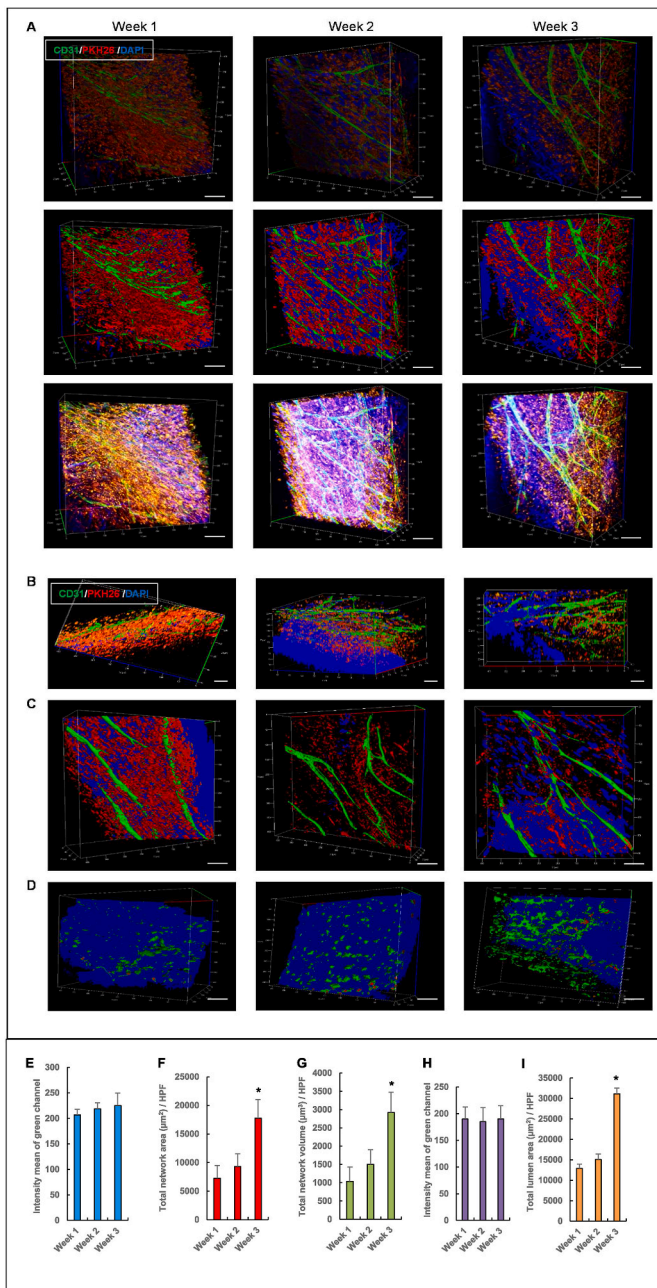
Fig. 7. Prevascularization of PDSF with perfusions of cocultured hASCs and HUVECs. (A) Two-photon excitation microscopy front views showed capillary-like structures in transparent (top panel), surface (middle panel), and maximum rendering views (bottom panel); these structures developed into a more interconnected network of vascular branches in PDSF from week 1 to week 2 and week 3. (B) Cross section views showed that the vascular network encapsulated (week 1–2) and then penetrated (week 3) the PDSF parenchyma. (C) The vascular tree became bigger, denser, and more complex along the re-endothelialized perforators, which arose from the pedicle, and spread throughout the matrix from week 1 to week 2 and week 3. (D) Main pedicle endothelialization increased with culturing time. The scale bars on the x-ases in A-D are 50 μm. (E–I) Imaging analysis revealed significant increases in the total area and volume of the endothelialized vessel network in PDSF (E–G) and in the endothelialized lumen area of the main pedicle (H&I). *$P < 0.05$ vs. week 1 and week 2. ANOVA was used for comparisons among multiple groups, as appropriate.

tissue and developed strong mechanical properties to adapt to the movement and enlargement of the abdominal wall as the animals grew and gained weight from 1 month to 3 months.

Several large blood vessel branches arising from the deep inferior epigastric artery grew into the grafts and were particularly distinct in the prevascularized PDSF group at 1 month and in both groups at 3 months (Fig. 9A–D). Dextran injected through the tail vein successfully circulated into the grafts, indicating the presence of functional blood vessels in the implants after surgery (Fig. 9E–L). Compared with PDSF, prevascularized PDSF had a significantly higher density of dextran-perfused medium blood vessels in both the interface area and center area at 1 month ($P < 0.05$) but not at 3 months (Fig. 9E-L). IHC staining confirmed that abundant CD31⁺ microvascular capillaries were distributed throughout the tissue sections; compared with PDSF, prevascularized PDSF had a significantly higher density of these vessels at 1 month ($P < 0.05$) (Fig. 9M–R). Given the presence of large and medium blood vessels and microvascular capillaries in the grafts, these data suggest that the grafts were successfully neovascularized and that prevascularization augmented the implants' neovascularization at an earlier time postoperatively.

As the biological implants neovascularized with the surrounding tissue, a foreign body reaction occurred. Macrophages are the key cells managing the destination of ECM-based implantation. A portion of the infiltrated cells in a PDSF graft was strongly positive for CD68 (all macrophages) and CD163 (M2 macrophages) but weakly positive for CD80 (M1 macrophages). Compared with PDSF, in which M2 macrophages were located mainly on the surface and in superficial layers, prevascularized PDSF had M2 macrophages distributed throughout, from the tissue-implant interface to the implant center (Fig. 9M − P). Both groups had high M2:M1 ratios, which were much greater in prevascularized PDSF than in PDSF ($P < 0.05$) (Fig. 9R). In contrast to PDSF, in prevascularized PDSF, the presence of hASCs contributed to the immunomodulation effect to significantly skew macrophages towards M2 polarization. In the normal skeletal muscle tissue, a few CD68⁺, CD163+, and CD80⁺ cells were observed, with slightly more CD163+ M2 macrophages than CD80⁺ M1 macrophages. This indicates that M2 macrophages are responsible for surveilling and maintaining homeostasis between pro-inflammation and anti-inflammation factors in muscle tissue (Fig. S3). Therefore, a foreign body reaction to a PDSF-based scaffold that is characterized by M2 macrophage predominance could provide a favorable microenvironment, inhibit inflammation, delay scaffold degradation, induce constructive remodeling, and promote musculofascial regeneration.

H&E and Masson trichrome staining revealed that PDSF grafts underwent uniform cell infiltration and that cells aligned along the fibril structures. Collagen was maintained as the main component in the grafts, and dense collagen bundles with oriented fibril structures were characteristic of mature fascia structures at 3 months (Fig. 9M − P). Many muscle tissues were distributed within the collagen matrix in both grafts; desmin and MyoD1 staining confirmed that in both groups, the numbers of these regenerated muscle bundles persisted with time. However, the grafts differed in how the cells were organized. In the PDSF implants, most desmin + cells were organized as thin aligned fibers near blood vessels. In contrast, in the prevascularized PDSF implants, abundant desmin + cells were organized as thick skeletal muscle islands; the overall histological score of desmin staining was also significantly higher at both time points ($P < 0.05$) (Fig. 9M–R). MyoD1, the myogenic marker expressed in muscle satellite cells, was detected in the interstitial tissue around the muscle bundles in grafts. Prevascularized PDSF had many more MyoD1+ cells than PDSF did ($P < 0.05$) (Fig. 9M–R). The characteristics of desmin and MyoD1 staining in the remodeled constructs coincided with the proteins' appearance in native skeletal muscle tissue, where abundant desmin was expressed in all muscle cell cytoplasm and MyoD1 was expressed in only muscle satellite cells (Fig. S3). These data indicate that PDSF implants underwent constructive remodeling and musculofascial regeneration and that
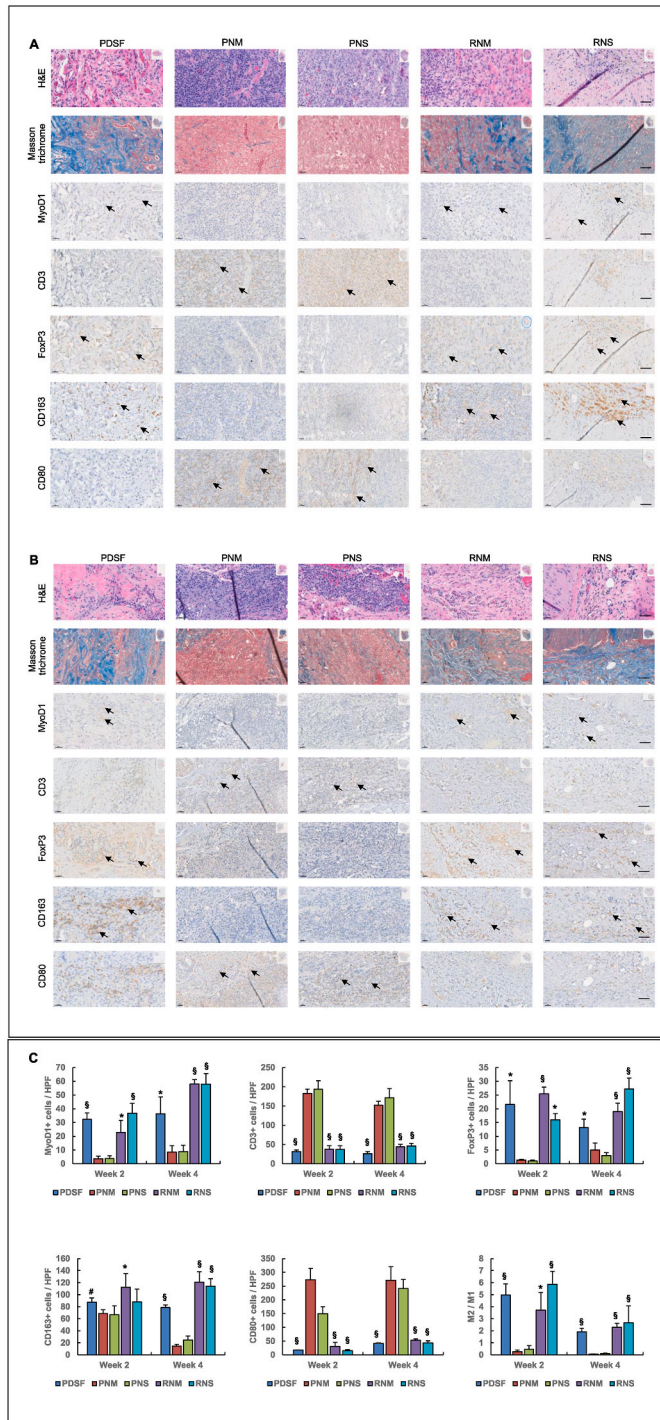
(caption on next column)

Fig. 8. Immunomodulatory properties of PDSF in a xenotransplantation model. IHC analysis indicated that the host accepted the PDSF graft without immunorejection 2 weeks (A) and 4 weeks (B) postoperatively. The pathobiological characteristics of PDSF xenotransplantation closely resembled those of the implantation of RNM and RNS from Fischer rats into syngeneic recipients in terms of inflammatory and immune cell infiltration and distribution. In these 3 groups, cellular infiltration occurred along with neovascularization from the peripheral area to the central area of the graft postoperatively. The implanted PDSF resulted in a foreign body reaction that was marked by the predominant infiltration of CD163+ M2 macrophages and FoxP3+ T-regs in the graft. The dominant presence of inflammatory M2 macrophages and T-regs induced the graft to undergo constructive remodeling, as evidenced by the myogenesis revealed by Masson trichrome and MyoD1 staining. Thirty days after the subcutaneously placement of PDSF, most of the graft was still collagen-based connective tissue undergoing myogenic regeneration. Compared with PDSF, RNM, and RNS, fresh xenografts from PNM and PNS stimulated strong immunorejection postoperatively, as evidenced by severe inflammation characterized by significant CD80$^+$ macrophage and CD3$^+$ T-cell infiltration that caused the graft to lose structure and disintegrate. Inset images indicate the areas shown in the magnified views. Black arrows indicate the positive stains of interest. The scale bars in A and B are 50 μm. (C) Differences in muscle regeneration, T-cell infiltration, and macrophage polarization among grafts. *$P < 0.05$ vs. each PNM and PNS at the same time point; §$P < 0.01$ vs. each PNM and PNS at the same time point; #$P < 0.05$ vs. PNM at week 2. The Student t-test was used for comparisons between 2 groups, as appropriate. ANOVA was used for comparisons among multiple groups, as appropriate.

prevascularization significantly improved the effectiveness of muscle regeneration. IHC with an anti-HuNu antibody revealed many pre-seeded human-derived cells within multiple layers of prevascularized PDSF at 1 month but much fewer such cells at 3 months (Fig. 9Q). These results suggest that engrafted hASCs, through paracrine action, influence the local environment rather than the differentiation of resident cells. Undoubtedly, the degradation of both the pre-seeded cells and bioscaffold, along with gradual constructive remodeling, are desirable attributes of muscle ECM-based scaffold-stem cell constructs used for musculofascial tissue engineering.

The remodeling outcome of PDSF was also similar to that of the positive control, RDMF (Fig. S4). As shown in Fig. S5, collagen-based connective tissue remained the main component of the explants at 3 months postoperatively. Desmin and MyoD1 staining confirmed the presence of regenerated muscle tissue along the collagen bundles. CD31$^+$ microvascular capillaries distributed throughout the tissue sections confirmed the grafts' neovascularization. CD68$^+$ macrophages infiltrated all explants. Compared with CD80$^+$ M1 macrophages, CD163+ M2 macrophages were the predominant subtype. These results closely resembled those observed in PDSF implantation constructive remodeling (Fig. 9M,O), which further highlights the myogenic properties of PDSF and its constructive remodeling ability *in vivo*.

4. Discussion

Tissue engineering, through the creation of living tissue constructs, remains the most appealing means of advancing reconstructive surgery. This approach avoids the incompatibility inherent to bioprosthetic options and averts the dangers of the immunosuppression and donor-related limitations inherent to other technologies such as vascularized composite tissue allotransplantation and autologous flaps [1–3,51]. Unfortunately, only modest progress has been made towards the realization of a clinically relevant engineered construct of any tissue type, including muscle tissue [29,30,52,53]. The timely establishment of a blood supply and the avoidance of immune-mediated damage after transplantation are important challenges in the use of large-scale TESM. We aimed to improve neovascularization and regenerative remodeling for TESM implantation by developing a muscle flap matrix, PDSF, from porcine stomach smooth muscle tissue. The unique characteristics and advantages of PDSF include its myoconductive and immunomodulatory
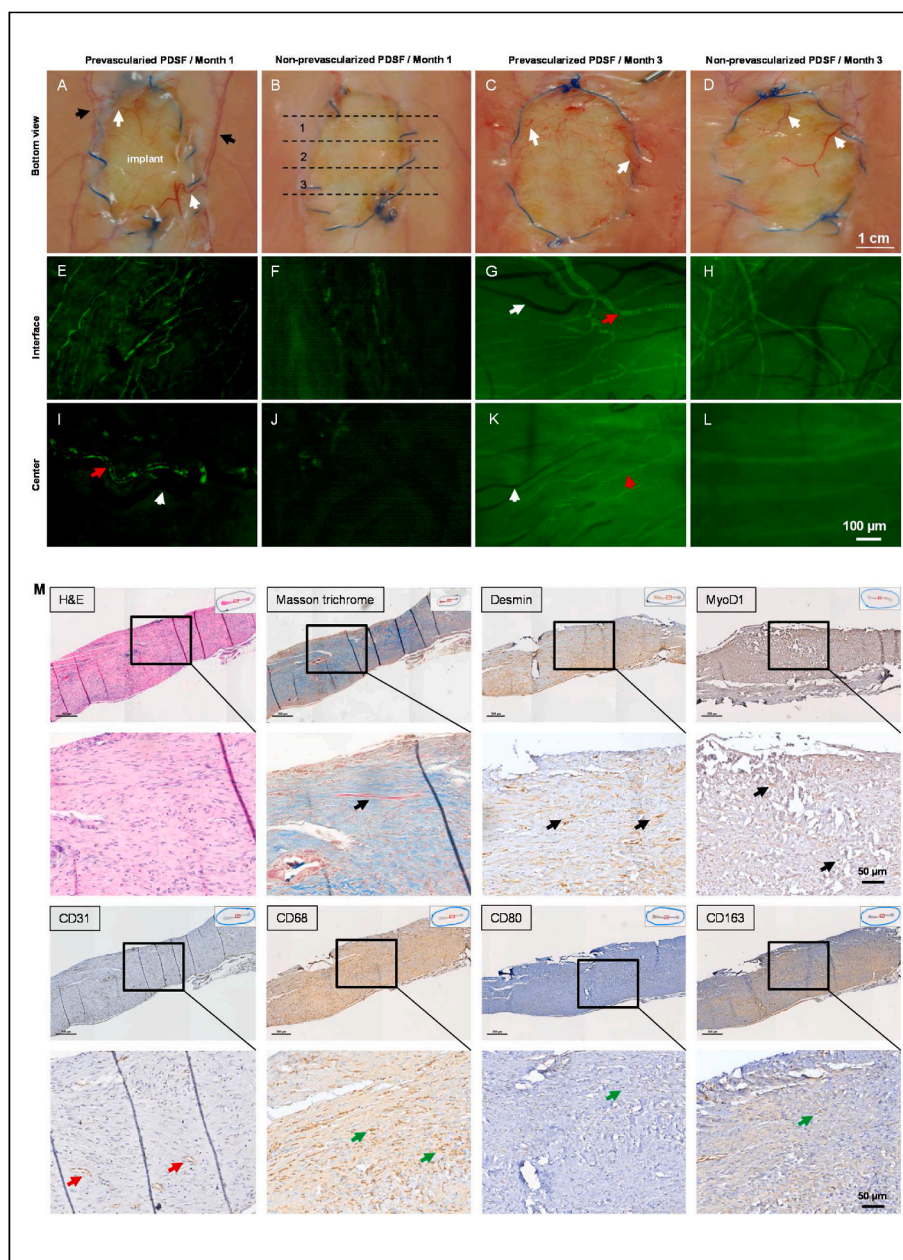
Fig. 9. Reconstruction of VML with prevascularized PDSF in a full-thickness abdominal wall defect model. (A–D) Morphologically the implants showed healing and integration with surrounding muscle tissue at 1 month and 3 months after surgery. Several communicating blood vessels (white arrows) arising from the deep inferior epigastric artery (black arrows) grew into the grafts; the numbers of these vessels were particularly increased in both groups at 3 months (C&D) and in the prevascularized PDSF group at 1 month (A). Explanted grafts were cut into 3 pieces, as indicated by the dashed lines; piece 2 was used for mechanical tests, and pieces 1 and 3 were used for IHC analysis (B). (E–L) Dextran-perfused functional blood vessels (green) revealed neovascularization in the grafts. At 1 month, the functional blood vessel density was significantly greater in prevascularized PDSF than in non-prevascularized PDSF. The numbers of these vessels continuously increased in both groups by 3 months. Red arrows indicate arteries; white arrows indicate veins. (M − P) IHC staining revealed remodeling of the central part of the non-prevascularized PDSF at 1 month (M) and 3 months (O) and remodeling of the central part of the prevascularized PDSF at 1 month (N) and 3 months (P). H&E and Masson trichrome staining 3 months after graft placement revealed that collagen-based connective tissue (blue) remained the main component of the grafts and that dense collagen bundles with oriented fibril structures were characteristic of mature fascia structures. In both types of grafts, many muscle tissues (pink) were distributed across the collagen matrix; desmin and MyoD1 staining (black arrows) confirmed these to be regenerated muscle bundles. Abundant desmin + cells aggregated as thick muscle islands in the prevascularized PDSF grafts (N&P). CD31^{+} microvascular capillaries (red arrows) distributed throughout the tissue sections confirmed the grafts' neovascularization. CD68^{+} macrophages (green arrows) infiltrated all explants. Compared with CD80^{+} M1 macrophages (green arrows), CD163+ M2 macrophages (green arrows) were the predominant subtype, especially in prevascularized PDSF (N&P). (Q) IHC with anti-HuNu antibodies was used to detect pre-seeded human cells in the prevascularized PDSF at 1 month. Most of these cells were hASCs (black arrows), and a few were HUVECs (red arrows) that presented in vascular structures. At 3 months, few pre-seeded human cells were detected, which suggests that most of these cells had degraded by this time. (R) Differences in muscle regeneration, blood vessel density, and macrophage polarization between non-prevascularized PDSF and prevascularized PDSF. *$P < 0.05$ vs. non-prevascularized PDSF at the same time point; §$P < 0.05$ vs. the same group at 1 month. The Student t-test was used for comparisons between 2 groups, as appropriate. ANOVA was used for comparisons among multiple groups, as appropriate. Inset images indicate the areas shown in the magnified views.
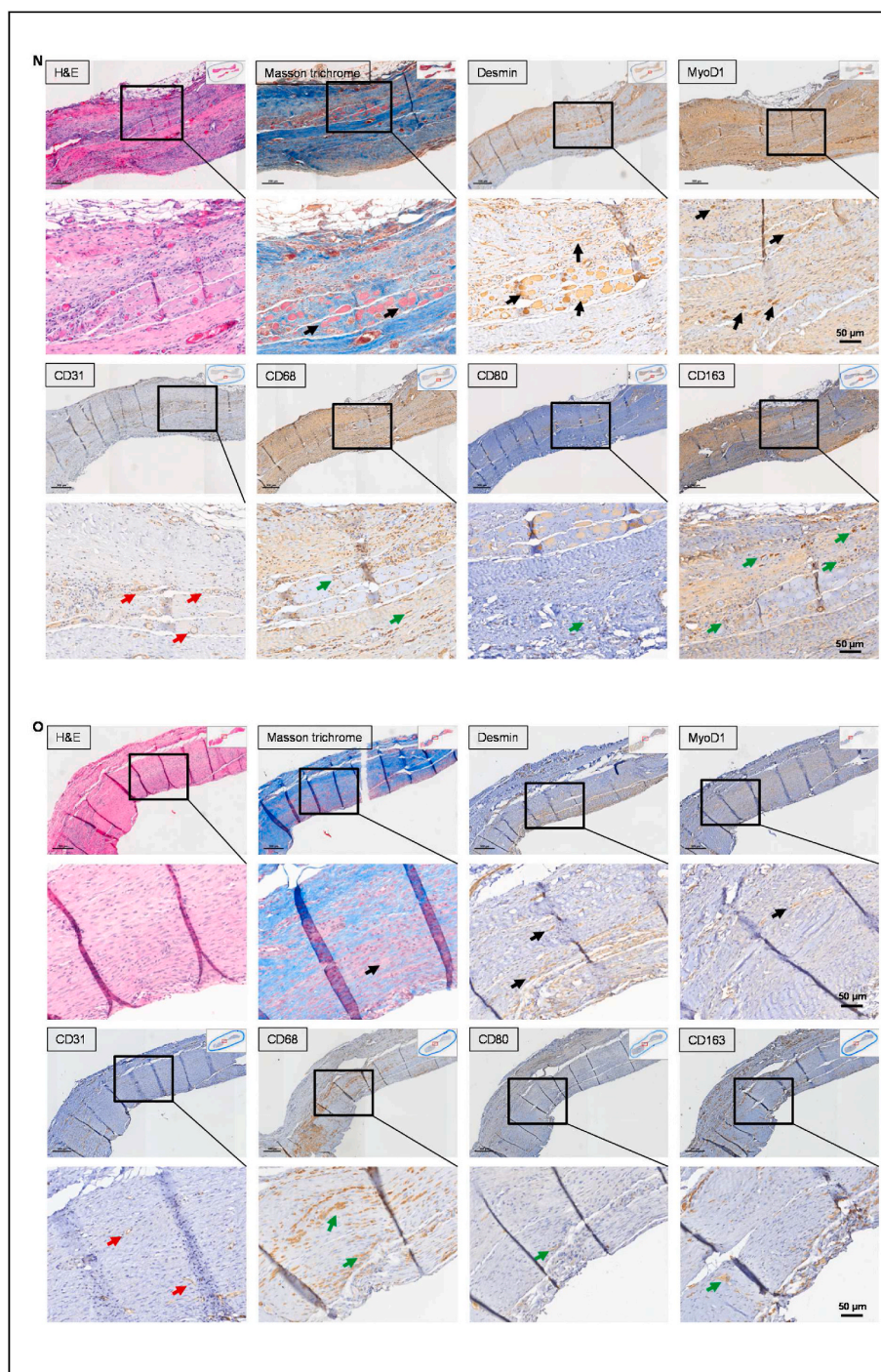
Fig. 9. (*continued*).

properties as well as its intact vasculature, which provides the structural basis for endothelialization and prevascularization by the perfusion seeding of hASCs and HUVECs. Our prevascularized PDSF-hASC construct not only augmented neovascularization but also modulated foreign body reactions, thus leading to constructive remodeling and muscle regeneration for VML reconstruction *in vivo*. Aided by their integration with PDSF, hASCs helped enhance both angiogenesis and immunomodulatory activities in our bioengineering approach.

In the present study, we applied a perfusion protocol combined with agitation to create the PDSF matrix. We found that this protocol efficiently removed cellular components from the muscle and vascular tissues. The resultant PDSF comprised multiple layers of musculofascial

ECM. Its well-maintained ECM architecture contained porous and tubular structures with nanofibrous features that resembled the characteristics of PDMM [32]. These topographical cues provided the 3D microenvironment necessary to direct muscle tissue−specific cellular behavior. PDSF supported the attachment, growth, and interconnection of hASCs, HUVECs, and HSMMs *in vitro*. In particular, compared with those cultured on 2D glass or 3D collagen gel, HSMMs cultured on PDSF were remarkably elongated, aligned, and interconnected; this tissue-specific manner of skeletal cell growth indicated improved muscle cell functionality. Furthermore, at the molecular level, in-depth LC-MS/MS analysis revealed that PDSF had 20 well-preserved matrisome proteins, including collagens, glycoproteins, proteoglycans, and
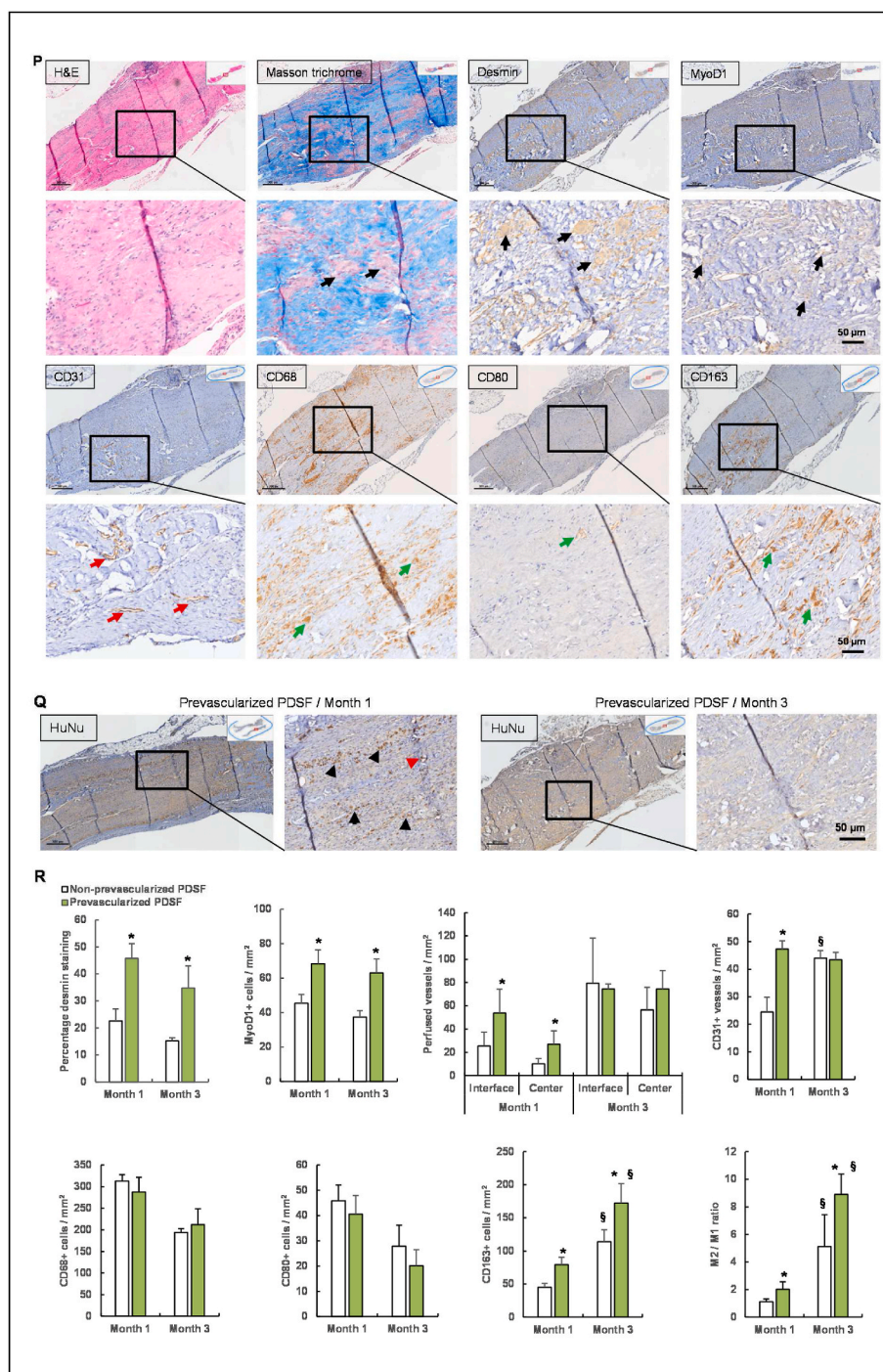
Fig. 9. (*continued*).

ECM regulators, indicating that the core matrisome of PDSF is highly similar to that of skeletal muscle. In addition, some common components of the matrisome belonged to different tissue ECM; such components included laminin γ, a major basement membrane constituent that plays important roles in a wide variety of biological processes, including cell adhesion, differentiation, and migration [54].

PDSF was also enriched in several proteins that are highly beneficial to muscle function and regeneration. For example, collagen V augments tissue generation and organoid formation [35], and collagen VI, which is primarily associated with the skeletal muscle ECM, maintains regularity in muscle function and stabilizes the cell membrane [36]. Our GO data

suggest that PDSF's proteomic profile represents a muscle ECM "zip code," which contributes to extracellular structure organization, collagen metabolic processes, muscle contraction, and muscle tissue morphogenesis. Coinciding with PDSF's support of skeletal muscle cells *in vitro*, the heterotopic (subcutaneous) and orthotopic (abdominal wall) xenotransplantation of PDSF *in vivo* yielded MyoD1+ and desmin + muscle tissue regeneration, further indicating that PDSF has important myoconductive properties. Different tissue types have distinct ECM compositions that might reflect the tissues' behaviors [40]. Our results suggest that the native 3D structural and biochemical properties of stomach muscle tissue ECM are well-maintained in PDSF and provide

molecular and topographical cues for cell repopulation and muscle tissue engineering and regeneration.

The biomaterials used in musculofascial tissue repair must be strong enough to withstand the mechanical forces experienced during and after surgery. The mechanical properties of PDSF were similar to those of PDFM and HDDM [32,55]. PDSF not only demonstrated strong mechanical properties but also had high strain at failure, which allows more flexibility and expandability, both of which are important for hernia repair and other types of VML repair. The 3D porous, tubular structure of PDSF favors cell infiltration, tissue remodeling, and integration. These features stand in contrast to those of acellular dermal matrix (ADM), which exhibits cell infiltration but not musculofascial regeneration [34,45]. Because small intestine submucosa (SIS), urinary bladder matrix (UBM) and ovine forestomach matrix (OFM) are usually very thin (around 0.5 mm per layer), they must be applied in multiple layers *in vivo*, which reduces their cost-effectiveness. We have investigated ADM from bench to bedside [34,45–47]; SIS, UBM and OFM derived from either submucosa (SIS), subepithelial lamina propria (UBM), or propria submucosa (OFM) without the ECM of muscularis layers, also have been widely studied by others [53,56–59], the advantages and disadvantages of these materials are well known. Therefore, the present study did not include them as controls. To our knowledge, no muscle-based ECM bioscaffolds are commercially available, and few ideal biologics for VML reconstruction are currently on the market [30,32,60]. As a muscle-based ECM biologic, PDSF could fill these gaps. Because PDSF is composed of a serosa extracellular matrix layer and 3 muscle extracellular matrix layers, it can be folded and adjusted as a composite sheet for personalized reconstruction. More importantly, PDSF has unique vascularity structures, which makes it suitable for prevascularization and flap engineering, thereby providing advantages over other options for VML reconstruction.

IHC analysis showed that PDSF is free from MHC I, MHC II, and α-gal xenoantigenicity, indicating that PDSF would be safe from rejection *in vivo*. Upon implantation, PDSF could activate a foreign body response mediated by host immune cells. There are two pathways of T-cell activation. One arises from the antigens presented by the graft's MHC, which is avoided in the case of PDSF, and the other arises from antigens presented by host APCs. After decellularization, PDSF retained some non-matrisome, or intracellular, proteins that are common to the ECM in other types of tissue, such as the pancreas [35], liver [41], vocal mucosa [42], and heart and skin [23,24,40]. The intracellular proteins, which may indicate lower allo- or xenoantigenicity, could be recognized by host APCs, which could present the proteins to T-cell receptors to activate a T-cell immune response to the foreign body [41]. However, T cells will remain nonfunctional if the antigen is presented at low levels or if insufficient costimulatory molecules (e.g., CD80, CD86) are present. In these situations, T cells could either became anergic or differentiate into T-regs, which secrete regulatory cytokines to prevent the activation of other T cells. T-regs (formerly known as suppressor T cells) are the most common mechanism of peripheral tolerance in transplantation [61,62]. The T-reg pathway could become activated in PDSF, as evidenced by the very few CD3^{+} T cells infiltrating the explants 30 days postoperatively in the Fischer rat xenotransplantation model. Moreover, more than half of the CD3^{+} T cells were recognized as FoxP3+ T-regs in the remodeled PDSF scaffold. In addition, instead of CD80^{+} M1 macrophages, CD163+ M2 macrophages were predominantly dispersed throughout the graft. These data indicate that abundant T cells can differentiate into T-regs (owing to lower levels of antigens and CD80 costimulatory molecules) or can be directly induced by M2 macrophages through CCL18-mediated pathways [63]. These data further suggest that PDSF has an important immunomodulatory property characterized by M2 macrophages and a host immune response dominated by T-regs. This property is important because it promotes graft acceptance upon implantation and drives an anti-inflammatory Th2 response that promotes constructive remodeling for tissue regeneration instead of severe fibrosis or the rapid degradation that results from rejection damage. The results of the present study are consistent with those of previous studies showing that human and porcine decellularized whole-ear scaffolds can induce a lower CD3^{+} T-cell response *in vivo* [22,23]. Previous studies have also shown that ECM scaffold can activate the M2 macrophage phenotype to support constructive remodeling [50,64–67]. Although the exact mechanisms by which ECM scaffold regulates macrophage polarization remain undefined, certain surface peptides and ligands on the scaffold that have been exposed by the decellularization process have been recognized to modulate the immune response [61,68,69]. ECM degradation products may also have immunomodulatory activity [7].

Because matrisome proteins play an important role in cell function *in vivo* [40], we focused on matrisome proteins in the present study. However, our LC-MS/MS analysis showed that the components of ECM scaffolds produced by current protocols are far more complex than expected. In particular, non-matrisome proteins are universally present in different ECM-based scaffolds [23,24,40–42], and the host response to these proteins is not fully understood. One recent study showed different host immune responses to multidomain peptides that have different chemical functionalities but similar nanostructural and mechanical properties [70]. Therefore, further investigation is needed to fundamentally understand ECM components' association with the subsequent host reaction and remodeling process *in vivo* to enable us to improve our ability to modify current decellularization protocols to eliminate unfavorable proteins or to enrich specific proteins for specific tissue-engineering purposes [71–74].

The use of hASCs combined with ECM-based scaffolds for tissue engineering has expanded substantially in recent years. In addition to having stem/progenitor properties, mesenchymal stem cells (MSCs) have broad immunoregulatory properties [63,75,76]. However, to our knowledge, the effects that hASC-loaded muscle ECM scaffolds have on macrophage phenotype transition, as well as the mechanisms underlying these effects, are largely unknown. Therefore, in this project, we identified the immunomodulatory effects of PDSF-hASC synergy on macrophage polarization by coculturing human CD14^{+} M0 macrophages with an hASC-seeded PDSF construct. We found that PDSF-hASC synergy significantly skewed M0 cells towards IL-10−producing CD206+ M2 macrophage polarization while significantly reducing their expression of HLA-DR and that the effect was associated with the constitutive increase in hASC-derived IL-6 levels that occurred when the hASCs were seeded on PDSF. We also found that the 3D culture system of the PDSF-hASC construct produced more growth factors, including TGF-β, EGF, and particularly VEGF and IGFBP, than hASCs in the 2D culture did. An aortic ring assay confirmed that these growth factors have biological functions in angiogenesis. These data indicate that the 3D topography cues of PDSF enhance hASCs' immunomodulatory effects on macrophage polarization as well as on the secretion of trophic mediators such as VEGF. Studies have shown that IL-6 and PGE2, which are produced by BM-MSCs and human umbilical cord−derived MSCs (UC-MSCs), are responsible for shifting M0 macrophages to M2 macrophages [49,77,78]. Studies have also suggested that the 3D environment is key to regulating the immunomodulatory effects of BM-MSCs that switch macrophages towards the anti-inflammatory M2 phenotype [79]. Because IL-6 derived from M1 macrophages is a pro-inflammatory cytokine, hASC-secreted IL-6 may play a role in a negative feedback loop to induce M0 macrophages towards the M2 phenotype in our system. As long as they were seeded on 3D PDSF, hASCs alone or in cocultures with HUVECs and/or HSMMs were able to produce higher levels of IL-6 (Fig. 5). These features ensured that hASCs, when applied with multiple cell types, executed their immunomodulatory functions to promote tissue engineering in an intricate environment. Compared with BM-MSCs, which have been studied extensively, ASCs are a relative new kind of MSC, and their immunoregulatory properties have not been fully investigated. We think ASCs share some common mechanisms with BM-MSCs or UC-MSCs for immunoregulation. Consistent with previous studies [49,77,78,80], our findings in the present study indicate that hASCs, when integrated with PDSF, can constitutively produce IL-6,

which polarizes M0 monocytes towards anti-inflammatory, IL-10–producing M2 macrophages. However, macrophage differentiation is a complex process involving numerous molecular cascades, and further study is needed to delineate the mechanism by which hASC-secreted IL-6 or other factors regulate molecular pathways to switch M0 macrophages to M2 macrophages. Our *in vitro* model involved only indirect contact between the PDSF-hASC construct and macrophages; to fully define the mechanisms by which hASCs modulate macrophage polarization, we plan to combine our model with direct-contact coculturing to investigate the cell signal transducers that mediate M2 macrophage differentiation in the PDSF microenvironment.

Coinciding with our *in vitro* findings, our investigation of the *in vivo* use of PDSF for rat VML repair showed that hASCs in prevascularized PDSF significantly induced macrophages towards the CD163+ M2 phenotype. Macrophages play an important role in determining the outcome of ECM-based construct implantation [7]. They initiate foreign body immune responses and surveil the process by adjusting the balance between the pro-inflammatory M1 and anti-inflammatory M2 pathways. M1 macrophages express high levels of IL-12, inducible nitric oxide synthase, and inflammatory cytokines such as IL-1β and TNF-α to induce a Th1-type inflammatory response. In contrast, M2 macrophages express high levels of IL-10 and TGF-β to induce a Th2-type anti-inflammatory response [81,82]. M2 macrophages help prevent muscle satellite cell apoptosis, and an essential step during skeletal muscle regeneration is the phenotypic switch of M1 macrophages to M2 macrophages [80,83, 84]. Our findings indicate that hASCs and PDSF work synergistically to activate M2 macrophage polarization and thus provide a pro-regenerative environment for muscle tissue formation *in vivo*.

Vascularization and blood supply are critical to the successful grafting of cell-biomaterial constructs. This is because oxygen diffusion is limited, allowing only the cells within 100–200 μm of the nearest capillary to survive, and spontaneous vascular ingrowth into the implant usually takes several days to weeks [6,85,86]. Hence, ischemia and hypoxia always lead to the necrosis or dysfunction of cell-biomaterial constructs, especially that of the cores of large-scale engineered constructs. Strategies to improve neovascularization within implanted bioscaffolds include introducing biochemical molecules, such as VEGF, to promote vessel formation [87]. Researchers have also incorporated physical components, such as nanofibrous structures, into scaffold design to induce neovascularization [88]. Coating the vascular network with biomolecules to promote endothelial cell adhesion and engraftment has also been investigated [89,90]. For example, a heparin-gelatin mixture has been used to endothelialize decellularized porcine liver [91]. Another strategy for increasing neovascularization involves cell-based treatment with MSCs and endothelial cells [6]. In the current project, we combined these multiple effective strategies to prevascularize PDSF. PDSF, which provides a 3D nanofibrous bioscaffold, is superior to synthetic materials because it eliminates the need to design vascular networks *de novo*. It also preserves the matrix's 3D native microcirculatory vascularity with a dominant vascular pedicle, which enables the coculturing of hASCs and HUVECs to engineer vascularized muscle tissue flaps. The intact rich vasculature of PDSF has several advantages: first, it facilitates decellularization; second, it accelerates cell seeding for recellularization and prevascularization; and third, it makes it feasible to perform pedicle anastomosis using microsurgery techniques to immediately establish a blood supply. In the present study, aided by the perfusion of cells seeded through the vascular tree, the dynamic coculturing of hASCs and HUVECs resulted in beautiful prevascularization in the PDSF, giving rise to networks of large and medium blood vessels and microvascular capillaries along the perforators. These vessel networks became more mature and complex with culture time. This *in vitro* vessel maturation is important to ensure the successful rapid anastomosis between the graft and host vasculatures *in vivo* [92]. This prevascularization likely resulted from both the endothelialization of preexisting vessel structures and the angiogenesis of new vessel branches. As confirmed in our *in vitro* model, hASCs play important roles

during prevascularization to stabilize and accelerate the attachment, proliferation, and engraftment of HUVECs through trophic factors such as VEGF [93]. Compared with PDSF, prevascularized PDSF resulted in better neovascularization and hence better constructive outcomes, as evidenced by the greater muscle regeneration in the VML model *in vivo*. This effectiveness was linked with the early establishment of a blood supply in the graft, which was achieved through the anastomosis of the graft's blood vessels with those in the surrounding tissue of the host, as illustrated by dextran perfusion. The improved neovascularization ensures the delivery of oxygen and nutrients to the large-scale biomaterial-cell construct, facilitating its survival and integration with the host while recruiting host bone marrow–derived immune cells and progenitor cells for tissue remodeling and regeneration [85,86,94]. As a result, immunomodulatory M2 macrophages dominated the host response, and desmin+ and MyoD1+ muscle satellite cells were significantly enriched in the prevascularized PDSF graft. These data demonstrate that hASCs, HUVECs, and myoconductive PDSF work together in a positive feedback loop to induce cell-construct constructive remodeling and muscle regeneration.

Muscle tissues have rich vasculature to meet their high metabolism demands. Previous studies have reported a prefabrication approach to implanting a vascular pedicle into matrices to engineer vascularized connective tissue pedicle flaps [95–98]. Those studies and the present study both recognized the close relationship between angiogenesis and tissue regeneration [99–101]. However, our ultimate goal is to engineer, *ex vivo,* a vascularized muscle-free flap whose clinical applicability is more flexible than that of pedicle flap. We tested our approach in a small animal model because the large diameter of the vascular pedicle of PDSF does not match those of rats' arteries. This work used a small animal model to acquire a proof-of-concept for applying prevascularized PDSF for muscle tissue reconstruction. Our animal model allowed the implantation of small grafts and was less technically demanding, which should enable us to rapidly and efficiently advance our technique to testing in large animal models. In vascularized composite muscle flap engineering, successful re-endothelialization of the composite muscle flap matrix is key to preventing thrombosis and achieving long-term transplantation survival in a large animal model (e.g., a porcine model). The vascular pedicle of PDSF provides an immediate blood supply after microsurgical anastomosis with recipient site vessels. Sufficient blood vessel network formation was achieved in the flap parenchyma and perforators; however, although the endothelialization of the main pedicle significantly increased during 3 weeks of culture, it remained incomplete.

As in whole-organ tissue engineering [102], complete re-endothelialization in vascularized composite tissue engineering presents several challenges [22–24]. One such challenge is that a large-scale flap matrix demands huge cell numbers for prepopulating both the vascular pedicle and parenchyma. Therefore, the optimization of bioreactor culture conditions for multiple cell types (e.g., ASCs, endothelial progenitor cells, and muscle progenitor cells) needs to be improved to enhance the cell engraftment of the PDSF *in vitro*. Current strategies might be improved by using induced pluripotent cells or protein-induced pluripotent stem cells derived from patients as alternative cell sources for clinical translational applications [103]. Another encouraging approach may be to combine partial *ex vivo* seeding and *in vivo* endothelialization of the flap [23], since even short-term blood perfusion could boost tissue survival and regeneration [18]. Another challenge is that functional muscle regeneration and reconstruction require nerve function rehabilitation [104]. The peripheral nerve structure in the flap matrix could easily bridge the host nerve growth into the flap [105]; we will investigate whether nerve function can fully recover in this setting and investigate the exciting methodologies mentioned above in our future studies of VML reconstruction in a porcine model.

5. Conclusions

We engineered a vascularized composite muscle tissue flap that can be sustained by its own microcirculatory network following microsurgical anastomosis with the host circulatory system and that can be constructively remodeled for muscle regeneration by the activation of preloaded stem cells. Such a flap could provide a clinically viable alternative to both autologous flaps and allogenic tissue flaps. We are the first to use a perfusion-based protocol to produce a porcine stomach smooth muscle flap matrix with well-maintained myoconductive ECM architecture that provides the molecular and topographical cues necessary for the integration and growth of hASCs, HSMMs, and HUVECs. We are also the first to demonstrate that PDSF-hASC synergy induces monocytes towards IL-10−producing M2 macrophage polarization via a feedback mechanism mediated by hASCs' paracrine effect and that PDSF-hASC synergy also promotes angiogenesis and vascular network formation and maturation *in vitro*. Our pre-vascularized, pre-cellularized muscle flap matrix, which includes both a dominant vascular pedicle and microcirculatory network and integrates multiple cell types, not only augments neovascularization but also modulates foreign-body reactions, thereby facilitating the constructive remodeling and long-term maintenance of muscle tissue regeneration *in vivo*. This approach provides a promising novel platform for composite muscle tissue free flap engineering and VML repair and reconstruction.

Ethics approval and consent to participate

All animal procedures were approved by the Institutional Animal Care and Use Committee at the University of Texas MD Anderson Cancer Center (#00000974-RN03). All clinical procedures were approved by MD Anderson's Institutional Review Board and performed in accordance with the institution's research guidelines (#PA17-0130-CR003). Written informed consent was obtained from all participants.

CRediT authorship contribution statement

Qixu Zhang: Conceptualization, Investigation, Methodology, Formal analysis, Resources, Funding acquisition, Supervision, Writing – original draft, Writing – review & editing. **Yulun Chiu:** Investigation, Methodology, Formal analysis. **Youbai Chen:** Investigation, Formal analysis. **Yewen Wu:** Investigation, Formal analysis. **Lina W. Dunne:** Investigation, Methodology, Formal analysis. **Rene D. Largo:** Investigation, Resources. **Edward I. Chang:** Investigation, Resources. **David M. Adelman:** Investigation, Resources. **Mark V. Schaverien:** Investigation, Resources. **Charles E. Butler:** Resources, Project administration.

Acknowledgments

Appendix A. Supplementary data

Supplementary data to this article can be found online at https://doi.org/10.1016/j.bioactmat.2022.10.023.

References

[1] J.T. Shores, G. Brandacher, W.P. Lee, Hand and upper extremity transplantation: an update of outcomes in the worldwide experience, Plast. Reconstr. Surg. 135 (2015) 351e–360e, https://doi.org/10.1097/PRS.0000000000000892.

[2] M. Kueckelhaus, S. Fischer, M. Seyda, E.M. Bueno, M.A. Aycart, M. Alhefz, A. ElKhal, B. Pomahac, S.G. Tullius, Vascularized composite allotransplantation: current standards and novel approaches to prevent acute rejection and chronic allograft deterioration, Transpl. Int. 29 (2016) 655–662, https://doi.org/10.1111/tri.12652.

[3] M. Siemionow, S. Nasir, Chimerism and bone marrow-based therapies in transplantation, Microsurgery 27 (2007) 510–521, https://doi.org/10.1002/micr.20395.

[4] M. Siemionow, T. Ortak, D. Izycki, R. Oke, B. Cunningham, R. Prajapati, J.E. Zins, Induction of tolerance in composite-tissue allografts, Transplantation 74 (2002) 1211–1217, https://doi.org/10.1097/00007890-200211150-00002.

[5] D. Gholobova, L. Terrie, M. Gerard, H. Declercq, L. Thorrez, Vascularization of tissue-engineered skeletal muscle constructs, Biomaterials 235 (2019), 119708, https://doi.org/10.1016/j.biomaterials.2019.119708.

[6] J. Rouwkema, N.C. Rivron, C.A. van Blitterswijk, Vascularization in tissue engineering, Trends Biotechnol. 26 (2008) 434–441, https://doi.org/10.1016/j.tibtech.2008.04.009.

[7] B.N. Brown, B.D. Ratner, S.B. Goodman, S. Amar, S.F. Badylak, Macrophage polarization: an opportunity for improved outcomes in biomaterials and regenerative medicine, Biomaterials 33 (2012) 3792–3802, https://doi.org/10.1016/j.biomaterials.2012.02.034.

[8] S.E. Hanson, R.N. D'Souza, P. Hematti, Biomaterial-mesenchymal stem cell constructs for immunomodulation in composite tissue engineering, Tissue Eng. A 20 (2014) 2162–2168, https://doi.org/10.1089/ten.tea.2013.0359.

[9] H.C. Ott, T.S. Matthiesen, S.K. Goh, L.D. Black, S.M. Kren, T.I. Netoff, D.A. Taylor, Perfusion-decellularized matrix: using nature's platform to engineer a bioartificial heart, Nat. Med. 14 (2008) 213–221, https://doi.org/10.1038/nm1684.

[10] H.C. Ott, B. Clippinger, C. Conrad, C. Schuetz, I. Pomerantseva, L. Ikonomou, D. Kotton, J.P. Vacanti, Regeneration and orthotopic transplantation of a bioartificial lung, Nat. Med. 16 (2010) 927–933, https://doi.org/10.1038/nm.2193.

[11] B.E. Uygun, A. Soto-Gutierrez, H. Yagi, M.L. Izamis, M.A. Guzzardi, C. Shulman, J. Milwid, N. Kobayashi, A. Tilles, F. Berthiaume, M. Hertl, Y. Nahmias, M. L. Yarmush, K. Uygun, Organ reengineering through development of a transplantable recellularized liver graft using decellularized liver matrix, Nat. Med. 16 (2010) 814–820, https://doi.org/10.1038/nm.2170.

[12] H. Mertsching, T. Walles, M. Hofmann, J. Schanz, W.H. Knapp, Engineering of vascularized scaffold for artificial tissue and organ generation, Biomaterials 26 (2005) 6610–6617, https://doi.org/10.1016/j.biomaterials.2005.04.048.

[13] D. Schultheiss, A.I. Gabouev, S. Cebotari, I. Tudorache, T. Walles, N. Schlote, J. Wefer, P.M. Kaufmann, A. Haverich, U. Jonas, C.G. Stief, H. Mertsching, Biological vascularized matrix for bladder tissue engineering: matrix preparation, reseeding technique and short-term implantation in a porcine model, J. Urol. 173 (2005) 276–280, https://doi.org/10.1097/01.ju.0000145882.80339.18.

[14] H. Mertsching, J. Schanz, V. Steger, M. Schandar, M. Schenk, J. Hansmann, I. Dally, G. Friedel, T. Walles, Generation and transplantation of an autologous vascularized bioartificial human tissue, Transplantation 88 (2009) 203–210, https://doi.org/10.1097/TP.0b013e3181ac15e1.

[15] H. Aubin, A. Kranz, J. Hülsmann, A. Pinto, M. Barth, A. Fomin, A. Lichtenberg, P. Akhyari, A novel native derived coronary artery tissue-flap model, Tissue Eng. C Methods 19 (2013) 970–980, https://doi.org/10.1089/ten.TEC.2012.0712.

[16] P.W. Henderson, V.V. Nagineni, A. Harper, N. Bavinck, A.M. Sohn, D.D. Krijgh, N. Jimenez, A.L. Weinstein, J.A. Spector, Development of an acellular bioengineered matrix with a dominant vascular pedicle, J. Surg. Res. 164 (2010) 1–5, https://doi.org/10.1016/j.jss.2010.07.017.

[17] J. Qu, R.M. Van Hogezand, C. Zhao, B.J. Kuo, B.T. Carlsen, Decellularization of a fasciocutaneous flap for use as a perfusable scaffold, Ann. Plast. Surg. 75 (2015) 112–116, https://doi.org/10.1097/SAP.0000000000000157.

[18] Q.X. Zhang, J.A. Johnson, L.W. Dunne, Y.B. Chen, T. Iyyanki, Y.W. Wu, E. I. Chang, C.D. Branch-Brooks, G.L. Robb, C.E. Butler, Decellularized skin/adipose tissue flap matrix for engineering vascularized composite soft tissue flaps, Acta Biomater. 35 (2016) 166–184, https://doi.org/10.1016/j.actbio.2016.02.017.

[19] B.J. Jank, J. Goverman, J.P. Guyette, J.M. Charest, M. Randolph, G.R. Gaudette, J.R. Gershlak, M. Purschke, E. Javorsky, R.M. Nazarian, D.A. Leonard, C. L. Cetrulo, W.G. Austen, H.C. Ott, Creation of a bioengineered skin flap scaffold with a perfusable vascular pedicle, Tissue Eng. A 23 (2017) 696–707, https://doi.org/10.1089/ten.TEA.2016.0487.

[20] G. Giatsidis, J.P. Guyette, H.C. Ott, D.P. Orgill, Development of a large-volume human-derived adipose acellular allogenic flap by perfusion decellularization, Wound Repair Regen. 26 (2018) 245–250, https://doi.org/10.1111/wrr.12631.

[21] B.J. Jank, L. Xiong, P.T. Moser, J.P. Guyette, X. Ren, C.L. Cetrulo, D.A. Leonard, L. Fernandez, S.P. Fagan, H.C. Ott, Engineered composite tissue as a bioartificial

limb graft, Biomaterials 61 (2015) 246–256, https://doi.org/10.1016/j.biomaterials.2015.04.051.

[22] J. Duisit, L. Maistriaux, A. Taddeo, G. Orlando, V. Joris, E. Coche, C. Behets, J. Lerut, C. Dessy, G. Cossu, E. Vögelin, R. Rieben, P. Gianell, B. Lengelé, Bioengineering a human face graft: the matrix of identity, Ann. Surg. 266 (2017) 754–764, https://doi.org/10.1097/SLA.0000000000002396.

[23] J. Duisit, H. Amiel, T. Wüthrich, A. Taddeo, A. Dedriche, V. Destoop, T. Pardoen, C. Bouzin, V. Joris, D. Magee, E. Vögelin, D. Harriman, C. Dessy, G. Orlando, C. Behets, R. Rieben, P. Gianello, B. Lengelé, Perfusion-decellularization of human ear grafts enables ECM-based scaffolds for auricular vascularized composite tissue engineering, Acta Biomater. 73 (2018) 339–354, https://doi.org/10.1016/j.actbio.2018.04.009.

[24] J. Duisit, G. Orlando, D. Debluts, L. Maistriaux, D. Xhema, Y.J. de Bisthoven, C. Galli, A. Peloso, C. Behets, B. Lengelé, P. Gianello, Decellularization of the porcine ear generates a biocompatible, Nonimmunogenic extracellular matrix platform for face subunit bioengineering, Ann. Surg. 267 (2018) 1191–1201, https://doi.org/10.1097/SLA.0000000000002181.

[25] M.M. Stern, R.L. Myers, N. Hammam, K.A. Stern, D. Eberli, S.B. Kritchevsky, S. Soker, M. Van Dyke, The influence of extracellular matrix derived from skeletal muscle tissue on the proliferation and differentiation of myogenic progenitor cells ex vivo, Biomaterials 30 (2009) 2393–2399, https://doi.org/10.1016/j.biomaterials.2008.12.069.

[26] J.A. DeQuach, J. Lin, C. Cam, D. Hu, M.A. Salvatore, F. Sheikh, K.L. Christman, Injectable skeletal muscle matrix hydrogel promotes neovascularization and muscle cell infiltration in a hindlimb ischemia model, Eur. Cell. Mater. 23 (2012) 400–412, https://doi.org/10.22203/ecm.v023a31.

[27] B. Perniconi, A. Costa, P. Aulino, L. Teodori, S. Adamo, D. Coletti, The pro-myogenic environment provided by whole organ scale acellular scaffolds from skeletal muscle, Biomaterials 32 (2011) 7870–7882, https://doi.org/10.1016/j.biomaterials.2011.07.016.

[28] M.T. Wolf, K.A. Daly, J.E. Reing, S.F. Badylak, Biologic scaffold composed of skeletal muscle extracellular matrix, Biomaterials 33 (2012) 2916–2925, https://doi.org/10.1016/j.biomaterials.2011.12.055.

[29] B.M. Sicari, J.P. Rubin, C.L. Dearth, M.T. Wolf, F. Ambrosio, M. Boninger, N. J. Turner, D.J. Weber, T.W. Simpson, A. Wyse, E.H. Brown, J.L. Dziki, L.E. Fisher, S. Brown, S.F. Badylak, An acellular biologic scaffold promotes skeletal muscle formation in mice and humans with volumetric muscle loss, Sci. Transl. Med. 6 (2014) 234–258, https://doi.org/10.1126/scitranslmed.3008085.

[30] B.T. Corona, S.M. Greising, Challenges to acellular biological scaffold mediated skeletal muscle tissue regeneration, Biomaterials 104 (2016) 238–246, https://doi.org/10.1016/j.biomaterials.2016.07.020.

[31] M. Bauer, E. Morales-Orcajo, L. Klemm, R. Seydewitz, V. Fiebach, T. Siebert, M. Böl, Biomechanical and microstructural characterisation of the porcine stomach wall: location- and layer-dependent investigations, Acta Biomater. 102 (2020) 83–99, https://doi.org/10.1016/j.actbio.2019.11.038.

[32] L. Wang, J.A. Johnson, D.W. Chang, Q.X. Zhang, Decellularized musculofascial extracellular matrix for tissue engineering, Biomaterials 34 (2013) 2641–2654, https://doi.org/10.1016/j.biomaterials.2012.12.048.

[33] T.S. Iyyanki, J. Hubenak, J. Liu, E.I. Chang, E.K. Beahm, Q.X. Zhang, Harvesting technique affects adipose-derived stem cell yield, Aesthetic Surg. J. 35 (2014) 467–476, https://doi.org/10.1093/asj/sju055.

[34] T.S. Iyyanki, L.W. Dunne, Q.X. Zhang, J. Hubenak, K.C. Turza, C.E. Butle, Adipose-derived stem-cell-seeded non-cross-linked porcine acellular dermal matrix increases cellular infiltration, vascular infiltration, and mechanical strength of ventral hernia repairs, Tissue Eng. A 21 (2015) 475–485, https://doi.org/10.1089/ten.TEA.2014.0235.

[35] H. Bi, K. Ye, S. Jin, Proteomic analysis of decellularized pancreatic matrix identifies collagen V as a critical regulator for islet organogenesis from human pluripotent stem cells, Biomaterials 233 (2020), https://doi.org/10.1016/j.biomaterials.2019.119673, 119673.

[36] P. Sabatelli, F. Gualandi, P. Bonaldo, L. Merlini, Detecting collagen VI in Bethlem myopathy, J. Biol. Chem. 290 (2015) 8011, https://doi.org/10.1074/jbc.L115.639088.

[37] J.C. Atkinson, M. Rühl, J. Becker, R. Ackermann, D. Schuppan, Collagen VI regulates normal and transformed mesenchymal cell proliferation in vitro, Exp. Cell Res. 228 (1996) 283–291, https://doi.org/10.1006/excr.1996.0328.

[38] P.D. Yurchenco, K.K. McKee, J.R. Reinhard, M.A. Rüegg, Laminin-deficient muscular dystrophy: molecular pathogenesis and structural repair strategies, Matrix Biol. 71 (2018) 174–187, https://doi.org/10.1016/j.matbio.2017.11.009.

[39] S.E. Gilpin, Q. Li, D. Evangelista-Leite, X. Ren, D.P. Reinhardt, B.L. Frey, H.C. Ott, Fibrillin-2 and Tenascin-C bridge the age gap in lung epithelial regeneration, Biomaterials 140 (2017) 212–219, https://doi.org/10.1016/j.biomaterials.2017.06.027.

[40] W. Han, N.K. Singh, J.J. Kim, H. Kim, B.S. Kim, J.Y. Park, J. Jang, D.W. Cho, Directed differential behaviors of multipotent adult stem cells from decellularized tissue/organ extracellular matrix bioinks, Biomaterials 224 (2019), 119496, https://doi.org/10.1016/j.biomaterials.2019.119496.

[41] Q. Li, B.E. Uygun, S. Geerts, S. Ozer, M. Scalf, S.E. Gilpin, H.C. Ott, M.L. Yarmush, L.M. Smith, N.V. Welham, B.L. Frey, Proteomic analysis of naturally-sourced biological scaffolds, Biomaterials 75 (2016) 37–46, https://doi.org/10.1016/j.biomaterials.2015.10.011.

[42] Q. Li, Z. Chang, G. Oliveira, M. Xiong, L.M. Smith, B.L. Frey, N.V. Welham, Protein turnover during in vitro tissue engineering, Biomaterials 81 (2016) 104–113, https://doi.org/10.1016/j.biomaterials.2015.12.004.

[43] S.F. Badylak, D.J. Weiss, A. Caplan, P. Macchiarini, Engineered whole organs and complex tissues, Lancet 379 (2012) 943–952, https://doi.org/10.1016/S0140-6736(12)60073-7.

[44] P.M. Crapo, T.W. Gilbert, S.F. Badylak, An overview of tissue and whole organ decellularization processes, Biomaterials 32 (2011) 3233–3243, https://doi.org/10.1016/j.biomaterials.2011.01.057.

[45] C.E. Butler, N.K. Burns, K.T. Campbell, A.B. Mathur, M.V. Jaffari, C.N. Rios, Comparison of cross-linked and non-cross-linked porcine acellular dermal matrices for ventral hernia repair, J. Am. Coll. Surg. 211 (2010) 368–376, https://doi.org/10.1016/j.jamcollsurg.2010.04.024.

[46] N.L. Nemeth, C.E. Butler, Complex torso reconstruction with human acellular dermal matrix: long-term clinical follow-up, Plast. Reconstr. Surg. 123 (2009) 192–196, https://doi.org/10.1097/PRS.0b013e3181934812.

[47] M. Asaad, S.K. Kapur, D.P. Baumann, J. Liu, C.E. Butler, Acellular dermal matrix provides durable long-term outcomes in abdominal wall reconstruction: a study of patients with over 60 Months of follow-up, Ann. Surg. (2020 Oct 19), https://doi.org/10.1097/SLA.0000000000004454.

[48] P.A. Zuk, M. Zhu, H. Mizuno, J. Huang, J.W. Futrell, A.J. Katz, P. Benhaim, H. P. Lorenz, M.H. Hedrick, Multilineage cells from human adipose tissue: implications for cell-based therapies, Tissue Eng. 7 (2001) 211–228, https://doi.org/10.1089/107632701300062859.

[49] S.M. Melief, S.B. Geutskens, W.E. Fibbe, H. Roelofs, Multipotent stromal cells skew monocytes towards an anti-inflammatory interleukin-10-producing phenotype by production of interleukin-6, Haematologica 98 (2013) 888–895, https://doi.org/10.3324/haematol.2012.078055.

[50] J.M. Fishman, M.W. Lowdell, L. Urbani, T. Ansari, A.J. Burns, M. Turmaine, J. North, P. Sibbons, A.M. Seifalian, K.J. Wood, M.A. Birchall, P. De Coppi, Immunomodulatory effect of a decellularized skeletal muscle scaffold in a discordant xenotransplantation model, Proc. Natl. Acad. Sci. U. S. A. 110 (2013) 14360–14365, https://doi.org/10.1073/pnas.1213228110.

[51] C.W. Patrick, R. Uthamanthil, E. Beahm, C. Frye, Animal models for adipose tissue engineering, Tissue Eng. B Rev. 14 (2008) 167–178, https://doi.org/10.1089/ten.teb.2007.0402.

[52] S.F. Badylak, J.L. Dziki, B.M. Sicari, F. Ambrosio, M.L. Boninger, Mechanisms by which acellular biologic scaffolds promote functional skeletal muscle restoration, Biomaterials 103 (2016) 128–136, https://doi.org/10.1016/j.biomaterials.2016.06.047.

[53] A. Aurora, J.L. Roe, B.T. Corona, T.J. Walters, An acellular biologic scaffold does not regenerate appreciable de novo muscle tissue in rat models of volumetric muscle loss injury, Biomaterials 67 (2015) 393–407, https://doi.org/10.1016/j.biomaterials.2015.07.040.

[54] P. Liu, H. Chen, L. Yan, Y. Sun, Laminin α5 modulates fibroblast proliferation in epidural fibrosis through the PI3K/AKT/mTOR signaling pathway, Mol. Med. Rep. 21 (2020) 1491–1500, https://doi.org/10.3892/mmr.2020.10967.

[55] A.S. Gobin, C.E. Butler, A.B. Mathur, Repair and regeneration of the abdominal wall musculofascial defect using silk fibroin-chitosan blend, Tissue Eng. 12 (2006) 3383–3394, https://doi.org/10.1089/ten.2006.12.3383.

[56] J. Zhang, G.Y. Wang, Y.P. Xiao, L.Y. Fan, Q. Wang, The biomechanical behavior and host response to porcine-derived small intestine submucosa, pericardium and dermal matrix acellular grafts in a rat abdominal defect model, Biomaterials 32 (2011) 7086–7095, https://doi.org/10.1016/j.biomaterials.2011.06.016.

[57] Z. Liu, Z. Yang, Z. Zhou, Z. Song, H. Wang, J. Yang, Host tissue integration process in abdominal wall defect repair: a comparison of two porcine-derived grafts in a long-term study, Expet Opin. Biol. Ther. 14 (2014) 883–892, https://doi.org/10.1517/14712598.2014.907783.

[58] S. Lun, S.M. Irvine, K.D. Johnson, N.J. Fisher, E.W. Floden, L. Negron, S. G. Dempsey, R.J. McLaughlin, M. Vasudevamurthy, B.R. Ward, B.C.H. May, A functional extracellular matrix biomaterial derived from ovine forestomach, Biomaterials 31 (2010) 4517–4529, https://doi.org/10.1016/j.biomaterials.2010.02.025.

[59] M.J. Smith, S.G. Dempsey, R.W.F. Veale, C.G. Duston-Fursman, C.A.F. Rayner, C. Javanapong, D. Gerneke, S.G. Dowling, B.A. Bosque, T. Karnik, M.J. Jerram, A. Nagarajan, R. Rajam, A. Jowsey, S. Cutajar, I. Mason, R.G. Stanley, A. Campbell, J. Malmstrom, C.H. Miller, B.C.H. May, Further structural characterization of ovine forestomach matrix and multi-layered extracellular matrix composites for soft tissue repair, J. Biomater. Appl. 36 (2022) 996–1010, http://doi.org/10.1177/08853282211045770.

[60] J. Zhang, Z. Hu, N.J. Turner, S. Teng, W. Cheng, H. Zhou, L. Zhang, H. Hu, Q. Wang, S.F. Badylak, Perfusion-decellularized skeletal muscle as a three-dimensional scaffold with a vascular network template, Biomaterials 89 (2016) 114–126, https://doi.org/10.1016/j.biomaterials.2016.02.040.

[61] P.L. Bollyky, B.A. Falk, R.P. Wu, J.H. Buckner, T.N. Wight, G.T. Nepom, Intact extracellular matrix and the maintenance of immune tolerance: high molecular weight hyaluronan promotes persistence of induced CD4+CD25+ regulatory T cells, J. Leukoc. Biol. 86 (2009) 567–572, https://doi.org/10.1189/jlb.0109001.

[62] P.L. Bollyky, R.P. Wu, B.A. Falk, J.D. Lord, S.A. Long, A. Preisinger, B. Teng, G. E. Holt, N.E. Standifer, K.R. Braun, C.F. Xie, P.L. Samuels, R.B. Vernon, J.A. Gebe, T.N. Wight, G.T. Nepom, ECM components guide IL-10 producing regulatory T-cell (TR1) induction from effector memory T-cell precursors, Proc. Natl. Acad. Sci. U. S. A. 108 (2011) 7938–7943, https://doi.org/10.5214/ans.0972.7531.180407.

[63] A.R. Weiss, M.H. Dahlke, Immunomodulation by mesenchymal stem cells (MSCs): mechanisms of action of living, apoptotic, and dead MSCs, Front. Immunol. 10 (2019) 1191, https://doi.org/10.3389/fimmu.2019.01191.

[64] B.A. St Pierre, J.G. Tidball, Differential response of macrophage subpopulations to soleus muscle reloading after rat hindlimb suspension, J. Appl. Physiol. 77 (1994) 290–297, https://doi.org/10.1152/jappl.1994.77.1.290.

[65] A. Malerba, L. Vitiello, D. Segat, E. Dazzo, M. Frigo, I. Scambi, P. De Coppi, L. Boldrin, L. Martelli, A. Pasut, C. Romualdi, R.G. Bellomo, J. Vecchiet, M. D. Baroni, Selection of multipotent cells and enhanced muscle reconstruction by myogenic macrophage-secreted factors, Exp. Cell Res. 315 (2009) 915–927, https://doi.org/10.1016/j.yexcr.2009.01.005.

[66] B.N. Brown, J.E. Valentin, A.M. Stewart-Akers, G.P. McCabe, S.F. Badylak, Macrophage phenotype and remodeling outcomes in response to biologic scaffolds with and without a cellular component, Biomaterials 30 (2009) 1482–1491, https://doi.org/10.1016/j.biomaterials.2008.11.040.

[67] D.M. Faulk, R. Londono, M.T. Wolf, C.A. Ranallo, C.A. Carruthers, J. D. Wildemann, C.L. Dearth, S.F. Badylak, ECM hydrogel coating mitigates the chronic inflammatory response to polypropylene mesh, Biomaterials 35 (2014) 8585–8595, https://doi.org/10.1016/j.biomaterials.2014.06.057.

[68] S.R. Morwood, L.B. Nicholson, Modulation of the immune response by extracellular matrix proteins, Arch. Immunol. Ther. Exp. (Warsz) 54 (2006) 367–374, https://doi.org/10.1007/s00005-006-0043-x.

[69] A.H. Thomas, E.R. Edelman, C.M. Stultz, Collagen fragments modulate innate immunity, Exp. Biol. Med. (Maywood, NJ, U. S.) 232 (2007) 406–411.

[70] T.L. Lopez-Silva, D.G. Leach, A. Azares, I.C. Li, D.G. Woodside, J.D. Hartgerink, Chemical functionality of multidomain peptide hydrogels governs early host immune response, Biomaterials 231 (2020), https://doi.org/10.1016/j.biomaterials.2019.119667, 119667.

[71] M.L. Wong, J.L. Wong, N. Vapniarsky, L.G. Griffiths, In vivo xenogeneic scaffold fate is determined by residual antigenicity and extracellular matrix preservation, Biomaterials 92 (2016) 1–12, https://doi.org/10.1016/j.biomaterials.2016.03.024.

[72] S.F. Badylak, The extracellular matrix as a biologic scaffold material, Biomaterials 28 (2007) 3587–3593, https://doi.org/10.1016/j.biomaterials.2007.04.043.

[73] J.M. Aamodt, D.W. Grainger, Extracellular matrix-based biomaterial scaffolds and the host response, Biomaterials 86 (2016) 68–82, https://doi.org/10.1016/j.biomaterials.2016.02.003.

[74] Z. Othman, B. Cillero Pastor, S. van Rijt, P. Habibovic, Understanding interactions between biomaterials and biological systems using proteomics, Biomaterials 167 (2018) 191–204, https://doi.org/10.1016/j.biomaterials.2018.03.020.

[75] M.E. Bernardo, W.E. Fibbe, Mesenchymal stromal cells: sensors and switchers of inflammation, Cell Stem Cell 13 (2013) 392–402, https://doi.org/10.1016/j.stem.2013.09.006.

[76] S.N. King, S.E. Hanson, X. Chen, J. Kim, P. Hematti, S.L. Thibeault, In vitro characterization of macrophage interaction with mesenchymal stromal cell-hyaluronan hydrogel constructs, J. Biomed. Mater. Res. A 102 (2014) 890–902, https://doi.org/10.1002/jbm.a.34746.

[77] S. Ghannam, J. Pène, G. Moquet-Torcy, C. Jorgensen, H. Yssel, Mesenchymal stem cells inhibit human Th17 cell differentiation and function and induce a T regulatory cell phenotype, J. Immunol. 185 (2010) 302–312, https://doi.org/10.4049/jimmunol.0902007.

[78] Z. Xie, H. Hao, C. Tong, Y. Cheng, J. Liu, Y. Pang, Y. Si, Y. Guo, L. Zang, Y. Mu, W. Han, Human umbilical cord-derived mesenchymal stem cells elicit macrophages into an anti-inflammatory phenotype to alleviate insulin resistance in type 2 diabetic rats, Stem Cell. 34 (2016) 627–639, https://doi.org/10.1002/stem.2238.

[79] G. Vallés, F. Bensiamar, L. Crespo, M. Arruebo, N. Vilaboa, L. Saldaña, Topographical cues regulate the crosstalk between MSCs and macrophages, Biomaterials 37 (2014) 124–133, https://doi.org/10.1016/j.biomaterials.2014.10.028.

[80] E. Pilny, R. Smolarczyk, M. Jarosz-Biej, A. Hadyk, A. Skorupa, M. Ciszek, Ł. Krakowczyk, N. Kułach, D. Gillner, M. Sokół, S. Szala, T. Cichoń, Human ADSC xenograft through IL-6 secretion activates M2 macrophages responsible for the repair of damaged muscle tissue, Stem Cell Res. Ther. 10 (2019) 93, https://doi.org/10.1186/s13287-019-1188-y.

[81] A. Mantovani, A. Sica, S. Sozzani, P. Allavena, A. Vecchi, M. Locati, The chemokine system in diverse forms of macrophage activation and polarization, Trends Immunol. 25 (2004) 677–686, https://doi.org/10.1016/j.it.2004.09.015.

[82] D.M. Mosser, J.P. Edwards, Exploring the full spectrum of macrophage activation, Nat. Rev. Immunol. 8 (2008) 958–969, https://doi.org/10.1038/nri2448.

[83] S. Carosio, L. Barberi, E. Rizzuto, C. Nicoletti, Z. Del Prete, A. Musarò, Generation of ex vivo-vascularized muscle engineered tissue (X-MET), Sci. Rep. 3 (2013) 1420, https://doi.org/10.1038/srep01420.

[84] N. Dumont, J. Frenette, Macrophages protect against muscle atrophy and promote muscle recovery in vivo and in vitro: a mechanism partly dependent on the insulin-like growth factor-1 signaling molecule, Am. J. Pathol. 176 (2010) 2228–2235, https://doi.org/10.2353/ajpath.2010.090884.

[85] M. Lovett, K. Lee, A. Edwards, D.L. Kaplan, Vascularization strategies for tissue engineering, Tissue Eng. B Rev. 15 (2009) 353–370, https://doi.org/10.1089/ten.TEB.2009.0085.

[86] O.C. Velazquez, Angiogenesis and vasculogenesis: inducing the growth of new blood vessels and wound healing by stimulation of bone marrow-derived progenitor cell mobilization and homing, J. Vasc. Surg. 45 (2007) A39–A47, https://doi.org/10.1016/j.jvs.2007.02.068.

[87] T. Shimizu, Cell sheet-based tissue engineering for fabricating 3-dimensional heart tissues, Circ. J. Adv. Pub. 78 (2014) 2594–2603, https://doi.org/10.1253/circj.cj-14-0973.

[88] F. Laco, M.H. Grant, R.A. Black, Collagen-nanofiber hydrogel composites promote contact guidance of human lymphatic microvascular endothelial cells and directed capillary tube formation, J. Biomed. Mater. Res. A 101 (2013) 1787–1799, https://doi.org/10.1002/jbm.a.34468.

[89] J. Devalliere, Y. Chen, K. Dooley, M.L. Yarmush, B.E. Uygun, Improving functional re-endothelialization of acellular liver scaffold using REDV cell-binding domain, Acta Biomater. 78 (2018) 151–164, https://doi.org/10.1016/j.actbio.2018.07.046.

[90] E. Dal Sasso, A. Zamuner, A. Filippi, F. Romanato, T. Palmosi, L. Vedovelli, D. Gregori, J.L. Gómez Ribelles, T. Russo, A. Gloria, L. Iop, G. Gerosa, M. Dettin, Covalent functionalization of decellularized tissues accelerates endothelialization, Bioact. Mater. 6 (2021) 3851–3864, https://doi.org/10.1016/j.bioactmat.2021.04.003.

[91] K.H. Hussein, K.M. Park, K.S. Kang, H.M. Woo, Heparin-gelatin mixture improves vascular reconstruction efficiency and hepatic function in bioengineered livers, Acta Biomater. 38 (2016) 82–93, https://doi.org/10.1016/j.actbio.2016.04.042.

[92] S. Ben-Shaul, S. Landau, U. Merdler, S. Levenberg, Mature vessel networks in engineered tissue promote graft-host anastomosis and prevent graft thrombosis, Proc. Natl. Acad. Sci. U. S. A. 116 (2019) 2955–2960, https://doi.org/10.1073/pnas.1814238116.

[93] D.O. Traktuev, S. Merfeld-Clauss, J. Li, M. Kolonin, W. Arap, R. Pasqualini, B. H. Johnstone, K.L. March, A population of multipotent CD34-positive adipose stromal cells share pericyte and mesenchymal surface markers, reside in a periendothelial location, and stabilize endothelial networks, Circ. Res. 102 (2008) 77–85, https://doi.org/10.1161/CIRCRESAHA.107.159475.

[94] S. Levenberg, J. Rouwkema, M. Macdonald, E.S. Garfein, D.S. Kohane, D. C. Darland, R. Marini, C.A. van Blitterswijk, R.C. Mulligan, P.A. D'Amore, R. Langer, Engineering vascularized skeletal muscle tissue, Nat. Biotechnol. 23 (2005) 879–884, https://doi.org/10.1038/nbt1109.

[95] Y. Shandalov, D. Egozi, J. Koffler, D. Dado-Rosenfeld, D. Ben-Shimol, A. Freiman, E. Shor, A. Kabala, S. Levenberg, An engineered muscle flap for reconstruction of large soft tissue defects, Proc. Natl. Acad. Sci. U. S. A. 111 (2014) 6010–6015, https://doi.org/10.1073/pnas.1402679111.

[96] A. Freiman, Y. Shandalov, D. Rosenfeld, E. Shor, D. Ben-David, S. Meretzki, S. Levenberg, D.J. Egozi, Engineering vascularized flaps using adipose-derived microvascular endothelial cells and mesenchymal stem cells, Tissue Eng. Regen. Med. 12 (2018) e130–e141, https://doi.org/10.1002/term.2436.

[97] T. Ismail, A. Lunger, A. Haumer, A. Todorov, N. Menzi, T. Schweizer, K. Bieback, J. Bürgin, D.J. Schaefer, I. Martin, A. Scherberich, Platelet-rich plasma and stromal vascular fraction cells for the engineering of axially vascularized osteogenic grafts, J. Tissue Eng. Regen. Med. 14 (2020) 1908–1917, https://doi.org/10.1002/term.3141.

[98] D. Steiner, S. Winkler, S. Heltmann-Meyer, V.T. Trossmann, T. Fey, T. Scheibel, R. E. Horch, A. Arkudas, Enhanced vascularization and de novo tissue formation in hydrogels made of engineered RGD-tagged spider silk proteins in the arteriovenous loop model, Biofabrication 13 (2021), 045003, https://doi.org/10.1088/1758-5090/ac0d9b.

[99] C. Epple, A. Haumer, T. Ismail, A. Lunger, A. Scherberich, D.J. Schaefer, I. Martin, Prefabrication of a large pedicled bone graft by engineering the germ for de novo vascularization and osteoinduction, Biomaterials 192 (2019) 118–127, https://doi.org/10.1016/j.biomaterials.2018.11.008.

[100] T. Osaki, V. Sivathanu, R.D. Kamm, Crosstalk between developing vasculature and optogenetically engineered skeletal muscle improves muscle contraction and angiogenesis, Biomaterials 156 (2018) 65–76, https://doi.org/10.1016/j.biomaterials.2017.11.041.

[101] Q.X. Zhang, J. Hubenak, T. Iyyanki, E. Alred, K.C. Turza, G. Davis, E.I. Chang, C. D. Branch-Brooks, E.K. Beahm, C.E. Butler, Engineering vascularized soft tissue flaps in an animal model using human adipose-derived stem cells and VEGF+ PLGA/PEG microspheres on a collagen-chitosan scaffold with a flow-through vascular pedicle, Biomaterials 73 (2015) 198–213, https://doi.org/10.1016/j.biomaterials.2015.09.024.

[102] K.H. Hussein, K.M. Park, L. Yu, S.H. Song, H.M. Woo, H.H. Kwak, Vascular reconstruction: a major challenge in developing a functional whole solid organ graft from decellularized organs, Acta Biomater. 103 (2020) 68–80, https://doi.org/10.1016/j.actbio.2019.12.029.

[103] H. Zhou, S. Wu, J.Y. Joo, S. Zhu, D.W. Han, T. Lin, S. Trauger, G. Bien, S. Yao, Y. Zhu, G. Siuzdak, H.R. Schöler, L. Duan, S. Ding, Generation of induced pluripotent stem cells using recombinant proteins, Cell Stem Cell 4 (2009) 381–384, https://doi.org/10.1016/j.stem.2009.04.005.

[104] J. Gilbert-Honick, S.R. Iyer, S.M. Somers, R.M. Lovering, K. Wagner, H.Q. Mao, W. L. Grayson, Engineering functional and histological regeneration of vascularized skeletal muscle, Biomaterials 164 (2018) 70–79, https://doi.org/10.1016/j.biomaterials.2018.02.006.

[105] M. Szynkaruk, S.W. Kemp, M.D. Wood, T. Gordon, G.H. Borschel, Experimental and clinical evidence for use of decellularized nerve allografts in peripheral nerve gap reconstruction, Tissue Eng. B Rev. 19 (2013) 83–96, https://doi.org/10.1089/ten.TEB.2012.0275.